Multidifferential cross section measurements of ν_μ-argon quasielasticlike reactions with the MicroBooNE detector

P. Abratenko,[35] O. Alterkait,[35] D. Andrade Aldana,[15] J. Anthony,[5] L. Arellano,[20] J. Asaadi,[34] A. Ashkenazi,[32] S. Balasubramanian,[12] B. Baller,[12] G. Barr,[25] J. Barrow,[21,32] V. Basque,[12] O. Benevides Rodrigues,[31] S. Berkman,[12] A. Bhanderi,[20] M. Bhattacharya,[12] M. Bishai,[3] A. Blake,[17] B. Bogart,[22] T. Bolton,[16] J. Y. Book,[14] L. Camilleri,[10] D. Caratelli,[4] I. Caro Terrazas,[9] F. Cavanna,[12] G. Cerati,[12] Y. Chen,[28] E. O. Cohen,[32] J. M. Conrad,[21] M. Convery,[28] L. Cooper-Troendle,[39] J. I. Crespo-Anadón,[6] M. Del Tutto,[12] S. R. Dennis,[5] P. Detje,[5] A. Devitt,[17] R. Diurba,[2] Z. Djurcic,[1] R. Dorrill,[15] K. Duffy,[25] S. Dytman,[26] B. Eberly,[30] A. Ereditato,[2] J. J. Evans,[20] R. Fine,[18] O. G. Finnerud,[20] W. Foreman,[15] B. T. Fleming,[39] N. Foppiani,[14] D. Franco,[39] A. P. Furmanski,[23] D. Garcia-Gamez,[13] S. Gardiner,[12] G. Ge,[10] S. Gollapinni,[33,18] O. Goodwin,[20] E. Gramellini,[12] P. Green,[20,25] H. Greenlee,[12] W. Gu,[3] R. Guenette,[20] P. Guzowski,[20] L. Hagaman,[39] O. Hen,[21] R. Hicks,[18] C. Hilgenberg,[23] G. A. Horton-Smith,[16] B. Irwin,[23] R. Itay,[28] C. James,[12] X. Ji,[3] L. Jiang,[37] J. H. Jo,[3,39] R. A. Johnson,[8] Y.-J. Jwa,[10] D. Kalra,[10] N. Kamp,[21] G. Karagiorgi,[10] W. Ketchum,[12] M. Kirby,[12] T. Kobilarcik,[12] I. Kreslo,[2] M. B. Leibovitch,[4] I. Lepetic,[27] J.-Y. Li,[11] K. Li,[39] Y. Li,[3] K. Lin,[27] B. R. Littlejohn,[15] W. C. Louis,[18] X. Luo,[4] C. Mariani,[37] D. Marsden,[20] J. Marshall,[38] N. Martinez,[16] D. A. Martinez Caicedo,[29] K. Mason,[35] A. Mastbaum,[27] N. McConkey,[20,36] V. Meddage,[16] K. Miller,[7] J. Mills,[35] A. Mogan,[9] T. Mohayai,[12] M. Mooney,[9] A. F. Moor,[5] C. D. Moore,[12] L. Mora Lepin,[20] J. Mousseau,[22] S. Mulleriababu,[2] D. Naples,[26] A. Navrer-Agasson,[20] N. Nayak,[3] M. Nebot-Guinot,[11] J. Nowak,[17] N. Oza,[10,18] O. Palamara,[12] N. Pallat,[23] V. Paolone,[26] A. Papadopoulou,[1,21] V. Papavassiliou,[24] H. B. Parkinson,[11] S. F. Pate,[24] N. Patel,[17] Z. Pavlovic,[12] E. Piasetzky,[32] I. D. Ponce-Pinto,[39] I. Pophale,[17] S. Prince,[14] X. Qian,[3] J. L. Raaf,[12] V. Radeka,[3] A. Rafique,[1] M. Reggiani-Guzzo,[20] L. Ren,[24] L. Rochester,[28] J. Rodriguez Rondon,[29] M. Rosenberg,[35] M. Ross-Lonergan,[18] C. Rudolf von Rohr,[2] G. Scanavini,[39] D. W. Schmitz,[7] A. Schukraft,[12] W. Seligman,[10] M. H. Shaevitz,[10] R. Sharankova,[12] J. Shi,[5] E. L. Snider,[12] M. Soderberg,[31] S. Söldner-Rembold,[20] J. Spitz,[22] M. Stancari,[12] J. St. John,[12] T. Strauss,[12] S. Sword-Fehlberg,[24] A. M. Szelc,[11] W. Tang,[33] N. Taniuchi,[5] K. Terao,[28] C. Thorpe,[17] D. Torbunov,[3] D. Totani,[4] M. Toups,[12] Y.-T. Tsai,[28] J. Tyler,[16] M. A. Uchida,[5] T. Usher,[28] B. Viren,[3] M. Weber,[2] H. Wei,[19] A. J. White,[39] Z. Williams,[34] S. Wolbers,[12] T. Wongjirad,[35] M. Wospakrik,[12] K. Wresilo,[5] N. Wright,[21] W. Wu,[12] E. Yandel,[4] T. Yang,[12] L. E. Yates,[12] H. W. Yu,[3] G. P. Zeller,[12] J. Zennamo,[12] and C. Zhang[3]

(MicroBooNE Collaboration)[*]

[1]*Argonne National Laboratory (ANL), Lemont, Illinois 60439, USA*
[2]*Universität Bern, Bern CH-3012, Switzerland*
[3]*Brookhaven National Laboratory (BNL), Upton, New York 11973, USA*
[4]*University of California, Santa Barbara, California 93106, USA*
[5]*University of Cambridge, Cambridge CB3 0HE, United Kingdom*
[6]*Centro de Investigaciones Energéticas, Medioambientales y Tecnológicas (CIEMAT), Madrid E-28040, Spain*
[7]*University of Chicago, Chicago, Illinois 60637, USA*
[8]*University of Cincinnati, Cincinnati, Ohio 45221, USA*
[9]*Colorado State University, Fort Collins, Colorado 80523, USA*
[10]*Columbia University, New York, New York 10027, USA*
[11]*University of Edinburgh, Edinburgh EH9 3FD, United Kingdom*
[12]*Fermi National Accelerator Laboratory (FNAL), Batavia, Illinois 60510, USA*
[13]*Universidad de Granada, Granada E-18071, Spain*
[14]*Harvard University, Cambridge, Massachusetts 02138, USA*
[15]*Illinois Institute of Technology (IIT), Chicago, Illinois 60616, USA*
[16]*Kansas State University (KSU), Manhattan, Kansas 66506, USA*
[17]*Lancaster University, Lancaster LA1 4YW, United Kingdom*
[18]*Los Alamos National Laboratory (LANL), Los Alamos, New Mexico 87545, USA*
[19]*Louisiana State University, Baton Rouge, Louisiana 70803, USA*
[20]*The University of Manchester, Manchester M13 9PL, United Kingdom*
[21]*Massachusetts Institute of Technology (MIT), Cambridge, Massachusetts 02139, USA*
[22]*University of Michigan, Ann Arbor, Michigan 48109, USA*
[23]*University of Minnesota, Minneapolis, Minnesota 55455, USA*
[24]*New Mexico State University (NMSU), Las Cruces, New Mexico 88003, USA*

[25]University of Oxford, Oxford OX1 3RH, United Kingdom
[26]University of Pittsburgh, Pittsburgh, Pennsylvania 15260, USA
[27]Rutgers University, Piscataway, New Jersey 08854, USA
[28]SLAC National Accelerator Laboratory, Menlo Park, California 94025, USA
[29]South Dakota School of Mines and Technology (SDSMT), Rapid City, South Dakota 57701, USA
[30]University of Southern Maine, Portland, Maine 04104, USA
[31]Syracuse University, Syracuse, New York 13244, USA
[32]Tel Aviv University, Tel Aviv, Israel, 69978
[33]University of Tennessee, Knoxville, Tennessee 37996, USA
[34]University of Texas, Arlington, Texas 76019, USA
[35]Tufts University, Medford, Massachusetts 02155, USA
[36]University College London, London WC1E 6BT, United Kingdom
[37]Center for Neutrino Physics, Virginia Tech, Blacksburg, Virginia 24061, USA
[38]University of Warwick, Coventry CV4 7AL, United Kingdom
[39]Wright Laboratory, Department of Physics, Yale University, New Haven, Connecticut 06520, USA

(Received 11 January 2023; accepted 12 July 2023; published 6 September 2023)

We report on a flux-integrated multidifferential measurement of charged-current muon neutrino scattering on argon with one muon and one proton in the final state using the Booster Neutrino Beam and MicroBooNE detector at Fermi National Accelerator Laboratory. The data are studied as a function of various kinematic imbalance variables and of a neutrino energy estimator, and are compared to a number of event generator predictions. We find that the measured cross sections in different phase-space regions are sensitive to nuclear effects. Our results provide precision data to test and improve the neutrino-nucleus interaction models needed to perform high-accuracy oscillation analyses. Specific regions of phase space are identified where further model refinements are most needed.

DOI: 10.1103/PhysRevD.108.053002

I. INTRODUCTION

High-precision measurements of the neutrino mixing angles, mass differences, and charge-parity violating phase, and the search for physics beyond the Standard Model are the primary physics goals of many currently operating as well as next-generation neutrino experiments [1–6]. These measurements require reliable comparisons of measured and theoretically expected neutrino interaction rates in the corresponding detectors. Thus, understanding the neutrino-nucleus scattering processes in detail is a prerequisite for these experiments to reach their discovery potential. A number of neutrino oscillation experiments employ liquid argon time projection chambers (LArTPCs) [3–5,7,8] to detect the particles produced in neutrino interactions. The ultimate goal of these efforts is both to reconstruct the energy of the neutrino based on the kinematics of the outgoing particles and to enable few-percent-level modeling of neutrino-argon interaction rates [9]. Therefore, high-accuracy modeling of neutrino-argon interactions is of the utmost importance [10–12].

This work presents the first measurement of flux-integrated single- and double-differential cross sections for muon-neutrino-argon (ν_μ-Ar) charged-current (CC) quasielastic (QE)-like scattering reactions as a function of kinematic imbalance variables [13–17]. Double-differential measurements as a function of a neutrino energy estimator are further reported for the first time in kinematic imbalance bins on argon. Motivated by a previous analysis with a similar signal event topology [18], we focus on reactions where a single muon-proton pair is reconstructed with no additional detected particles. The results reported here use the MicroBooNE detector [19] with an exposure of 6.79×10^{20} protons on target from the Booster Neutrino Beam (BNB) [20] at the Fermi National Accelerator Laboratory.

The experimental setup is presented in Sec. II, followed by the signal definition and event selection in Sec. III. The observables of interest are defined in Sec. IV. Section V describes the cross section extraction and systematics procedure, and Sec. VI outlines the modeling configurations used for comparison to the data. The results are reported in Sec. VII, and the conclusions are discussed in Sec. VIII.

II. EXPERIMENTAL SETUP

The MicroBooNE LArTPC has an active volume that contains 85 tonnes of argon. It is exposed to BNB

*microboone_info@fnal.gov

neutrinos, with an energy spectrum that peaks around 0.8 GeV and extends to 2 GeV.

Charged particles are produced after the primary neutrino interaction with the argon nuclei in the LArTPC active volume. Scintillation light and electron ionization trails are produced while these charged particles travel through the liquid argon. In the presence of an electric field of 273 V/cm, the ionization electrons drift toward a system of three anode wire planes. Photomultiplier tubes (PMTs) are used to measure the scintillation light.

If the PMT signals are in time coincidence with the beam arrival time, then events are recorded. Trigger hardware and software selection criteria are designed to minimize the contribution from background events, which are primarily cosmic muons. After these are applied, enriched data samples are obtained in which a neutrino interaction occurs in ≈15% of selected beam spills [21].

Individual particle tracks are reconstructed with Pandora pattern recognition algorithms based on the measured ionization signals in the enriched data samples [22]. Particles are identified based on the measured track energy deposition profile, while the particle momenta are obtained based on the track length [23,24].

III. SIGNAL DEFINITION & EVENT SELECTION

The QE-like signal definition used in this analysis includes all ν_μ-Ar scattering events with a final-state muon with momentum $0.1 < p_\mu < 1.2$ GeV/c, and exactly one proton with $0.3 < p_p < 1$ GeV/c. Events with final-state neutral pions at any momentum are excluded. Signal events may contain any number of protons below 300 MeV/c or above 1 GeV/c, neutrons at any momentum, and charged pions with momentum lower than 70 MeV/c. We refer to the events passing this definition as CC1p0π. The aforementioned momentum ranges are driven by considering resolution effects, as well as regions of the phase space with nonzero efficiencies and systematic uncertainties that are well understood. This signal consists predominantly of QE events. More complex interactions as labeled at a generator level, namely meson exchange currents (MEC), resonance interactions (RES) and deep inelastic scattering events (DIS), can still yield CC1p0π events. That can be the case due to final-state interactions (FSI), such as pion absorption, or due to the presence of particles outside the momentum range of interest in the CC1p0π signal definition as defined above.

Events that satisfy the CC1p0π signal definition at a reconstruction level but not at truth level are treated as background events. We refer to these events as non-CC1p0π. Based on simulation predictions, we find that the dominant background contribution originates from events with two protons in the momentum range of interest, where the second proton was not reconstructed. These events are referred to as CC1μ2p0π and are the focus of a dedicated MicroBooNE cross section analysis that demonstrated good data-simulation agreement [25].

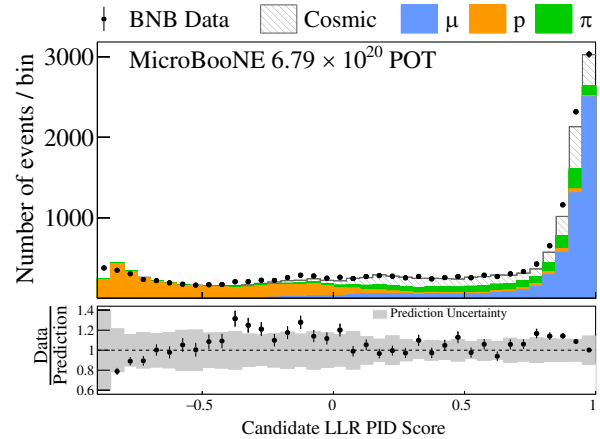

FIG. 1. The LLR PID score distribution used to tag the muon and proton candidates.

Candidate muon-proton pairs are isolated by requiring the existence of precisely two tracklike and no showerlike objects, as classified by Pandora using a track-score variable [26,27]. The log-likelihood ratio (LLR) particle identification (PID) score [28] is used to identify the muon and proton candidates. Figure 1 shows the particle composition breakdown of the sample as a function of the LLR PID score.

Muons tend to have higher LLR PID score values than protons; thus the track with the highest score is tagged as the candidate muon. Meanwhile, the track with the lower score is treated as the candidate proton.

Cosmic muon and non-CC1p0π contamination backgrounds were significantly reduced by applying a requirement on the candidate proton LLR PID score. We studied the effect of cutting on different values of this quantity, which has a strong discrimination power for rejecting MC non-CC1p0π background, out-of-cryostat and cosmic events. That yielded an optimal cut on the proton candidate LLR score of <0.05, as shown in Fig. 2(a). Figure 2(b) shows the corresponding muon candidate LLR score, which is peaked at values close to 1. The uncertainty bands account for potential data-MC discrepancies observed for both particle scores. The particle composition of the panels included in Fig. 2 is shown in the Supplemental Material [29].

To further minimize the contribution of misreconstructed track directions, we took advantage of two muon momentum reconstruction methods available for contained tracks, namely the momentum from range [30] and the momentum from Multiple Coulomb Scattering (MCS) [31]. The range and MCS muon momenta needed to be in agreement within 25%, and the improvement in the muon momentum reconstruction can be seen in Fig. 3. We required that the distance between the track start points and the vertex be smaller than the corresponding distance between the track end points and the vertex. We also demanded that the

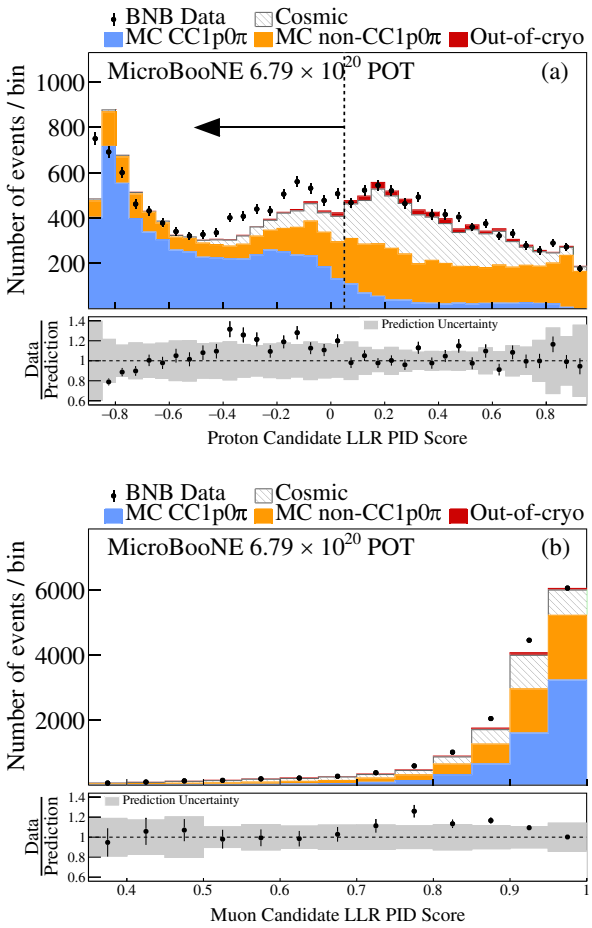

FIG. 2. (a) the proton candidate LLR PID score distribution, illustrating the fitness of a cut at LLR PID < 0.05 to reject cosmic and non-CC1p0π background events. (b) the muon candidate LLR PID score distribution, illustrating a peak close to 1. Only statistical uncertainties are shown in the data. The bottom panel shows the ratio of data to prediction.

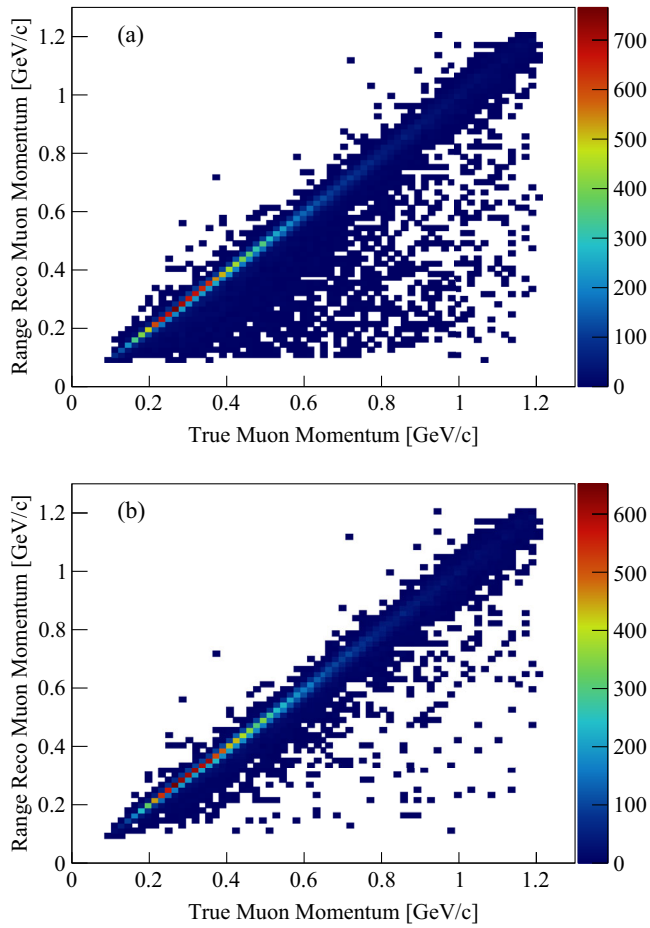

FIG. 3. Muon momentum reconstruction (a) before and (b) after the application of the muon momentum quality cut using contained muon tracks.

distance between the start points of the two candidate tracks be smaller than the distance between the two end points.

Further reduction of the cosmic tracks and minimization of bin-migration effects is achieved by considering only fully contained candidate muon-proton pairs within a fiducial volume of 10 cm inside the edge of the detector active volume. We retain 9051 data events that satisfy all event selection criteria.

In order to provide an accurate description of the dominant cosmic backgrounds pertinent to surface detectors, the full Monte Carlo (MC) simulation consists of a combination of simulated neutrino interactions overlaid on top of beam-off background data. This approach has been extensively used by MicroBooNE [18,32–34]. The GENIE v3.0.6 event generator is used to simulate neutrino interactions with the G18_10a_02_11a configuration [35,36]. The CCQE and CCMEC predictions have been additionally tuned to T2K ν_μ-carbon CC0π data with any number of protons in the final state [37,38]. The different target nuclei across T2K and MicroBooNE might result in particle reinteraction differences that can affect the reconstructed final-state topologies, such as different absorption effects. Yet, the T2K datasets used for tuning are dominated by CCQE and CCMEC interaction processes, which are the main contributors to the CC1p0π topology presented in this work. Predictions for more complex interactions, such as RES, remain unaltered, and no additional MC constraints are applied. We refer to the corresponding tuned prediction as G18. All the final-state particles following the primary neutrino interaction are generated by GENIE. They are further propagated in GENIE through the nucleus to account for FSI. The propagation of the particles outside the nucleus is simulated using GEANT4 [39]. The MicroBooNE detector response is modeled using the LArSoft framework [40,41]. Based on this MC prediction, we obtain a purity of $\approx$70% and an efficiency for selecting CC1p0π events of $\approx$10%. The final efficiency is primarily driven by the demand for exactly two fully contained tracklike candidates.

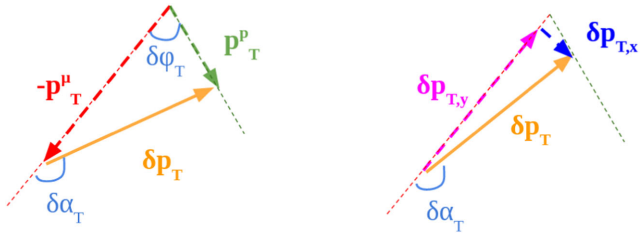

FIG. 4. Schematic representation of the kinematic imbalance variables on the plane transverse to the beam direction using CC1p0π events.

IV. OBSERVABLES

In neutrino-nucleus scattering events, there is an imbalance between the true initial neutrino momentum and the true sum of final-state lepton and hadron momenta as a result of nuclear effects [13]. A schematic representation of the kinematic imbalance variables of interest in this work is shown in Fig. 4.

Using the CC1p0π candidate muon-proton pair kinematics, the missing momentum in the plane transverse to the beam direction is defined as

$$\delta p_T = |\vec{p}_T{}^{\mu} + \vec{p}_T{}^{p}|, \tag{1}$$

where $\vec{p}_T{}^{\mu}$ and $\vec{p}_T{}^{p}$ are the projections of the momenta of the outgoing lepton and proton on the transverse plane, respectively. In the absence of nuclear effects, purely QE interactions would yield $\delta p_T = 0$. In the presence of the dense nuclear medium, this variable encapsulates information related to the Fermi motion, but it is smeared due to FSI and non-QE interactions, as can be seen in Fig. 5.

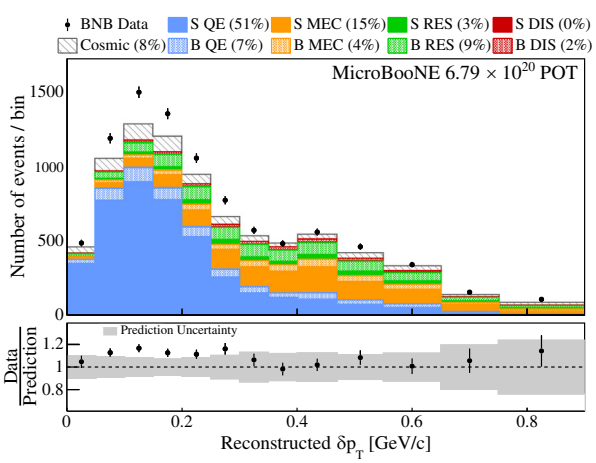

FIG. 5. Distribution of the selected CC1p0π events as a function of the transverse missing momentum δp_T. Only statistical uncertainties are shown in the data. The interaction contributions are obtained from simulation, and their separation in signal (S) and background (B) events is presented. The bottom panel shows the ratio of data to prediction.

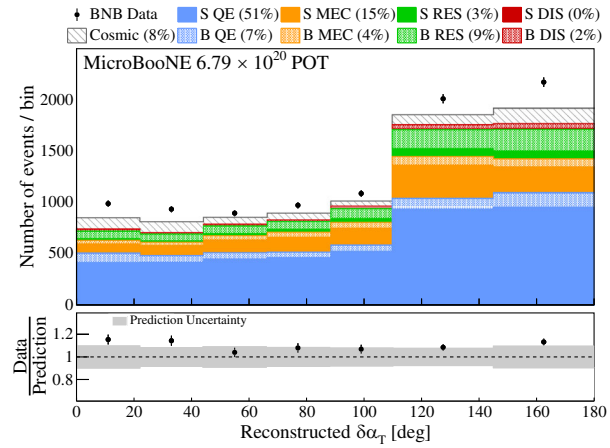

FIG. 6. Distribution of the selected CC1p0π events as a function of the transverse missing momentum direction $\delta\alpha_T$. Only statistical uncertainties are shown in the data. The interaction contributions are obtained from simulation, and their separation in signal (S) and background (B) events is presented. The bottom panel shows the ratio of data to prediction.

Further discussion on the FSI smearing effects can be found in Sec. VII.

The direction of the transverse momentum imbalance δp_T is described by the angle

$$\delta\alpha_T = \arccos\left(\frac{-\vec{p}_T{}^{\mu}\cdot\delta\vec{p}_T}{p_T{}^{\mu}\delta p_T}\right), \tag{2}$$

which is uniformly distributed in the absence of FSI due to the isotropic nature of the Fermi motion. In the presence of FSI, the proton momentum is generally reduced, and the $\delta\alpha_T$ distribution becomes weighted toward 180°, as can be seen in Fig. 6.

The opening angle $\delta\phi_T$ between the correlated candidate muon-proton pair on the transverse plane is given by

$$\delta\phi_T = \arccos\left(\frac{-\vec{p}_T{}^{\mu}\cdot\vec{p}_T{}^{p}}{p_T{}^{\mu}p_T{}^{p}}\right). \tag{3}$$

In the absence of nuclear effects, QE events would be concentrated at $\delta\phi_T = 0$. When nuclear effects are present, QE events can occupy wider angles. At the same time, non-QE events are dominant in the high $\delta\phi_T$ part of the tail, and their contribution is fairly flat across all angles, as can be seen in Fig. 7.

The muon-proton momentum imbalances transverse and longitudinal to the transverse lepton momentum [16] are defined as

$$\begin{aligned}\delta p_{T,x} &= (\hat{p}_\nu \times \hat{p}_T^{\mu})\cdot\delta\vec{p}_T\\ \delta p_{T,y} &= -\hat{p}_T^{\mu}\cdot\delta\vec{p}_T,\end{aligned} \tag{4}$$

and can also be written as

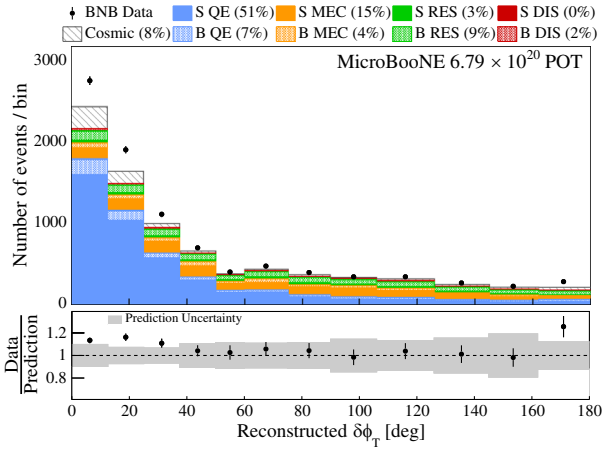

FIG. 7. Distribution of the selected CC1p0π events as a function of the muon-proton transverse opening angle $\delta\phi_T$. Only statistical uncertainties are shown in the data. The interaction contributions are obtained from simulation, and their separation in signal (S) and background (B) events is presented. The bottom panel shows the ratio of data to prediction.

$$\delta p_{T,x} = \delta p_T \cdot \sin\delta\alpha_T$$
$$\delta p_{T,y} = \delta p_T \cdot \cos\delta\alpha_T. \tag{5}$$

These distributions can be seen in Figs. 8 and 9, respectively. The $\delta p_{T,x}$ distribution is symmetric around 0 GeV/c due to the presence of the $\sin\delta\alpha_T$ factor in Eq. (5) and the fact that $\delta\alpha_T$ ranges from 0° to 180°. The width of the distribution is driven by the Fermi motion that affects the δp_T magnitude. Unlike $\delta p_{T,x}$, the $\delta p_{T,y}$ distribution is asymmetric with an enhanced contribution from negative

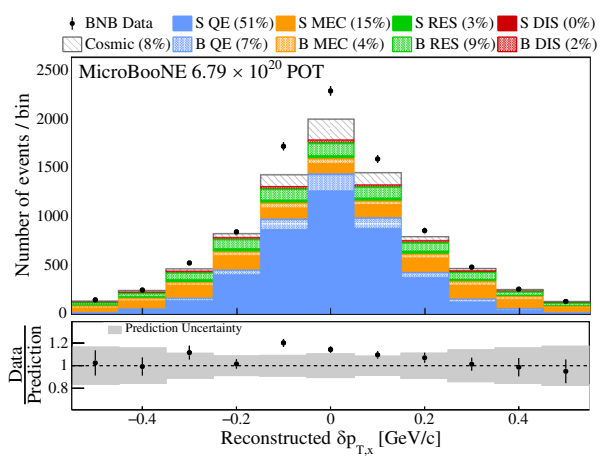

FIG. 8. Distribution of the selected CC1p0π events as a function of the perpendicular component of the transverse missing momentum $\delta p_{T,x}$. Only statistical uncertainties are shown in the data. The interaction contributions are obtained from simulation, and their separation in signal (S) and background (B) events is presented. The bottom panel shows the ratio of data to prediction.

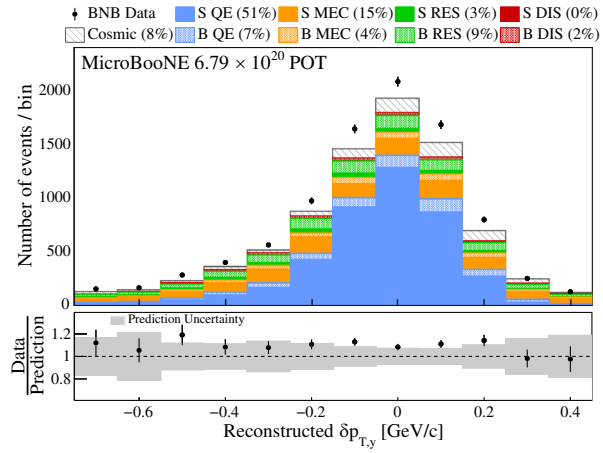

FIG. 9. Distribution of the selected CC1p0π events as a function of the longitudinal component of the transverse missing momentum $\delta p_{T,y}$. Only statistical uncertainties are shown in the data. The interaction contributions are obtained from simulation, and their separation in signal (S) and background (B) events is presented. The bottom panel shows the ratio of data to prediction.

values. The asymmetry is driven by the presence of the $\cos\delta\alpha_T$ factor in Eq. (5) and the fact that $\delta\alpha_T$ is mainly peaked around 180°. Given that the forward $\delta\alpha_T$ peak is driven by FSI, the size of the $\delta p_{T,y}$ asymmetry is also sensitive to the FSI strength.

Finally, the calorimetric energy reconstruction

$$E^{\mathrm{Cal}} = E_\mu + T_p + BE \tag{6}$$

is investigated, where E_μ is the muon energy, T_p is the proton kinetic energy and $BE = 0.04$ GeV is the average binding energy for argon [42]. This energy estimator, shown in Fig. 10, is an approximation for the true energy of the incoming neutrino and is used in oscillation searches.

V. CROSS SECTION EXTRACTION & SYSTEMATICS

The flux-averaged differential event rate as a function of a given variable x in bin i is obtained by

$$\frac{dR}{dx_i} = \frac{N_i - B_i}{T \cdot \Phi_\nu \cdot \Delta_i} \tag{7}$$

where N_i and B_i are the number of measured events and the expected background events, respectively. T is the number of target argon nuclei in the fiducial volume of interest. Φ_ν corresponds to the integrated BNB flux, and Δ_i corresponds to the ith bin width or area for the single- and double-differential results, respectively.

We report the extracted cross sections for CC1p0π interactions using the Wiener singular value decomposition (Wiener-SVD) unfolding technique as a function of unfolded kinematic variables [43]. This unfolding procedure corrects a

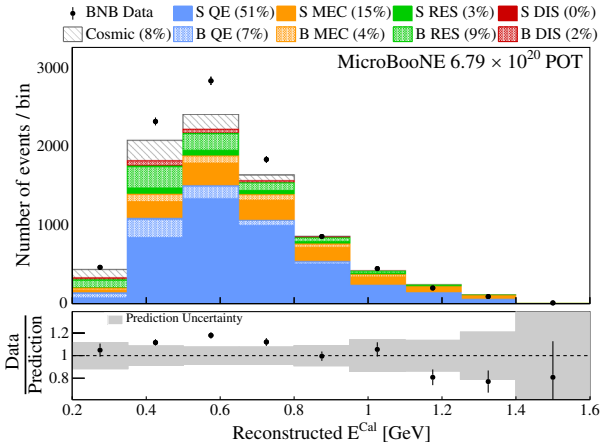

FIG. 10. Distribution of the selected CC1p0π events as a function of the calorimetric energy reconstruction E^{Cal}. Only statistical uncertainties are shown in the data. The interaction contributions are obtained from simulation, and their separation in signal (S) and background (B) events is presented. The bottom panel shows the ratio of data to prediction.

measured event rate for inefficiency and resolution effects. This is achieved by performing a minimization of a χ^2 score that compares data to a prediction and allows for a regularization term. A Wiener filter determines the level of regularization that is required to minimize the mean square error between the variance and bias of the result. In addition to the measured event rate, the method uses a covariance matrix calculated from simulated events accounting for the statistical and systematic uncertainties on the measurement as input. It also requires the construction of a response matrix describing the expected detector smearing and reconstruction efficiency.

The output of the method is an unfolded differential cross section, a covariance matrix describing the total uncertainty on the unfolded result, and an additional smearing matrix that we refer to as A_C. The latter contains information about the regularization and bias of the measurement. The corresponding A_C matrices have been applied to all the cross section predictions included in this work when a comparison to the unfolded data is performed. The A_C matrix should be applied to any independent theoretical prediction when a comparison is performed to the data reported in this paper. The data release, the unfolded covariance matrices, and the additional matrices A_C can be found in the Supplemental Material [29].

The total covariance matrix $E_{ij} = E_{ij}^{\mathrm{stat}} + E_{ij}^{\mathrm{syst}}$ includes the statistical and systematic uncertainties on the differential event rate associated with our measurement. E_{ij}^{stat} is a diagonal covariance matrix with the statistical uncertainties, and E_{ij}^{syst} is a covariance matrix that incorporates the total systematic uncertainties both on the CC1p0π signal and on the non-CC1p0π background events as detailed below.

The neutrino flux is predicted using the flux simulation of the MiniBooNE collaboration that used the same beam line [44]. Neutrino cross section modeling uncertainties were estimated using the GENIE framework of event reweighting [35,36,38]. The rescattering uncertainties were obtained using GEANT4 and the relevant reweighting package [45]. For each of these sources of uncertainty, we use a multisim technique [46], which consists of generating a large number of MC replicas, each one called a "universe," where model parameters are varied within their uncertainties. The simultaneous varying of many model parameters provides a correct treatment of their correlations. A total of n such universes are used to construct a covariance matrix corresponding to each source of uncertainty,

$$E_{ij} = \frac{1}{n}\sum_{k=1}^{k=n}(R_i^k - R_i^{CV})\cdot(R_j^k - R_j^{CV}) \tag{8}$$

where R_i^{CV} (R_j^{CV}) and R_i^k (R_j^k) are the flux-averaged event rates for the central value and systematic universe k in a measured bin i (j), respectively. The resulting covariance matrices are summed together to estimate the relevant uncertainty from each source.

In order to account for potential biases due to the nominal MC modeling prediction used in the unfolding procedure and presented in Sec. VI, an additional cross section uncertainty using the NuWro v19.02.2 event generator prediction [47] as an alternative universe has been added. The relevant NuWro modeling is significantly different when compared with the nominal MC one, as detailed in Sect. VI. The flux-integrated NuWro cross sections are obtained using Eq. (7), and the corresponding covariance matrices are constructed using Eq. (8) and a single universe ($n = 1$).

For detector model systematic uncertainties, one detector parameter is varied each time by 1σ and is referred to as a "unisim." These include variations in the light yield, the ionization electron recombination model, space-charge effects, and waveform deconvolution [48]. We then examine the impact of each parameter variation on the MC event rates by obtaining the differences with respect to the central value on a bin-by-bin basis. We define the total detector 1σ systematic uncertainty by summing in quadrature the effect of m detector variations using the formalism introduced in Eq. (8),

$$E_{ij} = \sum_{k=1}^{k=m}(R_i^k - R_i^{CV})\cdot(R_j^k - R_j^{CV}). \tag{9}$$

The full fractional uncertainty on the integrated total cross section is 11% and includes contributions from the neutrino flux prediction (7.3%), neutrino interaction cross section modeling (6%), detector response modeling (4.9%), beam exposure (2.3%), statistics (1.5%), number-of-scattering targets (1.2%), reinteractions (1%), and out-of-cryostat (dirt)

interaction modeling (0.2%). The Supplemental Material [29] includes tables detailing all the cross section uncertainties used in this work. The main contributors are found to be the strength of the RPA correction and CCMEC cross section shape. The signal related cross section uncertainties are found to be 8.6%, while the background ones account for 6.3%. Note that the individual contributions are higher than the total cross section uncertainty of 6% due to correlations between the signal and background events, since the same interaction processes can contribute both as signal and background.

In the results presented below, the inner error bars on the reported cross sections correspond to the statistical uncertainties. The systematic uncertainties were decomposed into shape- and normalization-related sources following the procedure outlined in [49]. The cross-term uncertainties were incorporated in the normalization part. The outer error bars on the reported cross sections correspond to statistical and shape uncertainties added in quadrature. The normalization uncertainties are presented with the gray band at the bottom of each plot. Overflow (underflow) values are included in the last (first) bin. The relevant A_C matrices have been applied to the theoretical predictions to account for regularization effects.

VI. MODELING CONFIGURATIONS

The nominal MC neutrino interaction prediction (G18) uses the local Fermi gas (LFG) model [50], the Nieves CCQE scattering prescription [51] which includes Coulomb corrections for the outgoing muon [52] and random phase approximation (RPA) corrections [53]. Additionally, it uses the Nieves MEC model [54], the KLN-BS RES [55–58] and Berger-Sehgal (BS) coherent (COH) [59] scattering models, the hA2018 FSI model [60], and MicroBooNE-specific tuning of model parameters [38].

Our results are also compared to a number of alternative event generators. GiBUU 2021 (GiBUU) uses similar models, but they are implemented in a coherent way by solving the Boltzmann-Uehling-Uhlenbeck transport equation [61]. The modeling includes the LFG model [50], a standard CCQE expression [62], an empirical MEC model and a dedicated spin dependent resonance amplitude calculation following the MAID analysis [61]. The DIS model is from PYTHIA [63]. GiBUU's FSI treatment propagates the hadrons through the residual nucleus in a nuclear potential which is consistent with the initial state. NuWro v19.02.2 (NuWro) uses the LFG model [50], the Llewellyn Smith model for QE events [64], the Nieves model for MEC events [65], the Adler-Rarita-Schwinger formalism to calculate the Δ resonance explicitly [58], the BS COH [59] scattering model and an intranuclear cascade model for FSI [65]. NEUT v5.4.0 (NEUT) uses the LFG model [50], the Nieves CCQE scattering prescription [51], the Nieves MEC model [54], the BS RES [55–58] and BS COH [59] scattering models, and FSI with Oset medium corrections for pions [35,36].

In addition to the alternative event generators, our results are compared to a number of different GENIE configurations. These include an older version, GENIE v2.12.10 (Gv2) [35,36], which uses the Bodek-Ritchie Fermi Gas model, the Llewellyn Smith CCQE scattering prescription [64], the empirical MEC model [66], a Rein-Sehgal RES and COH scattering model [67], and a data driven FSI model denoted as "hA" [68]. Another model, "Untuned," uses the GENIE v3.0.6 G18_10a_02_11a configuration without additional MicroBooNE-specific tuning. Finally, the newly added theory-driven GENIE v3.2.0 G21_11b_00_000 configuration (G18) is shown. This includes the SuSAv2 prediction for the QE and MEC scattering parts [69] and the hN2018 FSI model [70]. The modeling options for RES, DIS, and COH interactions are the same as for G18.

To quantify the data-simulation agreement, the χ^2/bins ratio data comparison for each generator is shown on all the figures and is calculated by taking into account the total covariance matrix. Ratios close to unity are indicative of a sufficiently accurate modeling performance. Theoretical uncertainties on the models themselves are not included.

VII. RESULTS

Along with the aforementioned kinematic imbalance and energy estimator results, the data are also presented as a function of the lepton angular orientation (Fig. 11). Previous MicroBooNE measurements using different signal definitions [18,71,72] showed discrepancies in that quantity, primarily in the forward direction. These analyses used an older simulation prediction, namely GENIE v2.12.2, to account for the efficiency corrections and beam-induced backgrounds. This work illustrates that all generator [Fig. 11(a)] and GENIE configuration [Fig. 11(b)] predictions are in good agreement with the data when reported as a function of $\cos\theta_\mu$.

Figures 12 and 13 show the measured single-differential cross sections as a function of δp_T using all the events [panel (a)], as well as the double-differential results as a function of the same kinematic variable in $\delta\alpha_T$ bins [panels (b)–(e)]. In the presence of FSI, the proton can rescatter or be absorbed, yielding larger kinematic imbalances on the transverse plane and δp_T values that extend beyond the Fermi momentum, as can be seen in Fig. 14. Furthermore, the same extended tail can be obtained when pions produced due to multinucleon effects (MEC or RES) are either absorbed or below the detection threshold. The single-differential result shows such a high-momentum tail that extends above 0.8 GeV/c. This picture is consistent with the results reported by the T2K and MINERvA Collaborations [14,15,73]. Unlike the single-differential result, the double-differential results with low $\delta\alpha_T$ extend only slightly above 0.4 GeV/c. That indicates that this

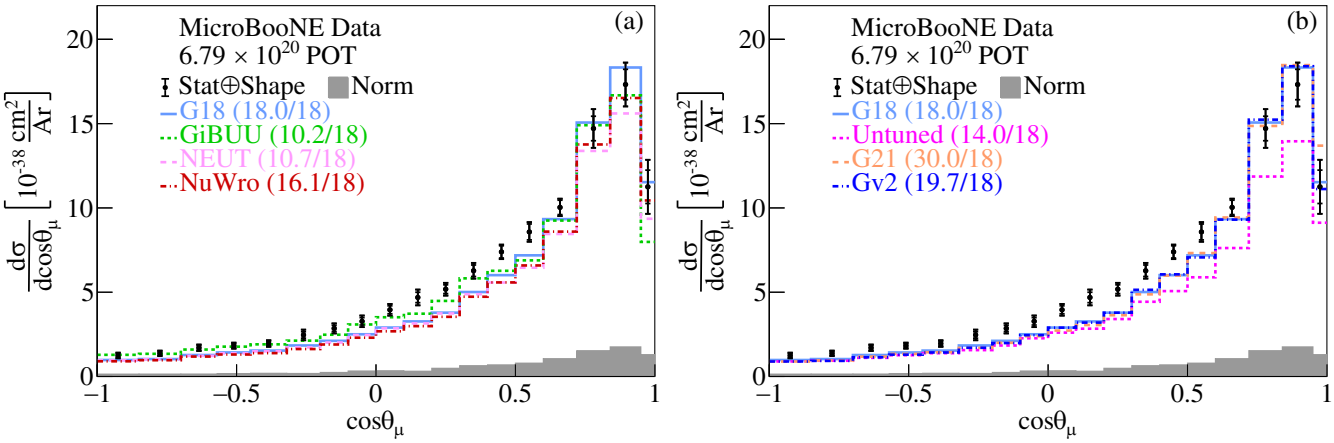

FIG. 11. The flux-integrated single-differential cross sections as a function of $\cos\theta_\mu$. (a) Generator and (b) GENIE configuration predictions are compared to data. Inner and outer error bars show the statistical and total (statistical and shape systematic) uncertainty at the 1σ, or 68%, confidence level. The gray band shows the normalization systematic uncertainty. The numbers in parentheses show the χ^2/bins calculation for each one of the predictions.

region contains minimal FSI and multinucleon effects and the δp_T distribution is driven by the nucleon Fermi motion. On the other hand, the higher $\delta\alpha_T$ values correspond to δp_T distributions that extend beyond 0.8 GeV/c. This behavior is indicative of the presence of FSI and multinucleon effects that smear the δp_T distribution to higher values. Future multidifferential results can help further disentangle the contributions from these effects. Figure 12 shows the comparisons to a number of available neutrino event generators with NuWro and G18 showing the best agreement over all events. Figure 13 shows the same results compared to a number of GENIE configurations illustrating that Gv2 is disfavored, an observation that is driven by the Gv2 low δp_T behavior. Furthermore, Untuned shows a good χ^2/bins performance across all slices but predicts lower values than the data. Additionally, Fig. 14 shows the effect of FSI on the CC1p0π selection using the G18 configuration of GENIE. The addition of FSI allows for more non-QE events to satisfy the CC1p0π signal definition that smears the δp_T distribution to higher values.

Figure 15 shows the double-differential results as a function of δp_T in $\cos\theta_\mu$ bins. In a factorized nuclear model such as the LFG, the Fermi motion part of δp_T should stay constant in terms of the shape as a function of the outgoing lepton kinematics, since in such models the initial state nucleon momentum is a property of the nucleus that cannot be affected by the interaction momentum or energy transfer. That is indeed the observed behavior in the reported results across all event generators and configurations, where no evidence of the inadequacy of the factorization approach is observed. Figure 15 shows the comparisons to a number of available neutrino event generators, where the G18 prediction is favored based on the χ^2/ndf results. Apart from the factorization, a better separation between QE and non-QE can be gained depending on the $\cos\theta_\mu$ region. As can be seen in Fig. 16 for G18, MEC events play a more pronounced role for forward muon scattering and in the high δp_T tail, as opposed to backward scattering angles, which are much more strongly populated by QE events. Furthermore, the G18 cross section prediction falls below the data in the $-1 < \cos\theta_\mu < 0.5$ region, as seen in Figs. 16(a) and 16(b). That could indicate that additional contribution from the QE part of the G18 prediction is needed beyond the MicroBooNE tune. Figure 17 shows the same interaction breakdown for GiBUU. Unlike G18, GiBUU illustrates a peak shift to the right, which becomes more pronounced in the backward direction. This shift is driven by the enhanced MEC contribution in higher δp_T values and the reduced QE contribution at smaller values. In the backward direction, GiBUU further shows a cross section excess driven by the MEC contribution. Figure 18 shows the same results compared to a number of GENIE configurations illustrating that Gv2 is disfavored due to the low δp_T bin behavior.

Figures 19 and 20 show the double-differential cross section as a function of δp_T in $\cos\theta_p$ bins. The factorization of the nuclear motion is mostly preserved in $\cos\theta_p$ bins, analogously to the previous result in $\cos\theta_\mu$. Figure 19 shows the comparisons to a number of available neutrino event generators. The GiBUU prediction is significantly lower than the data in the backward proton angle for low δp_T values, as shown in Fig. 19(a). Figure 20 shows the same results compared to a number of GENIE configurations illustrating that Gv2 is disfavored across all $\cos\theta_p$ bins. As can be seen in Fig. 21, this particularly poor performance is driven by the QE contribution. For backward scattering events [panel (a)], the QE contribution predicted by Llewellyn Smith is significantly overestimated. For intermediate angles ($0 < \cos\theta_p < 0.5$), the same QE model results in an unphysical double peak. For forward scattering

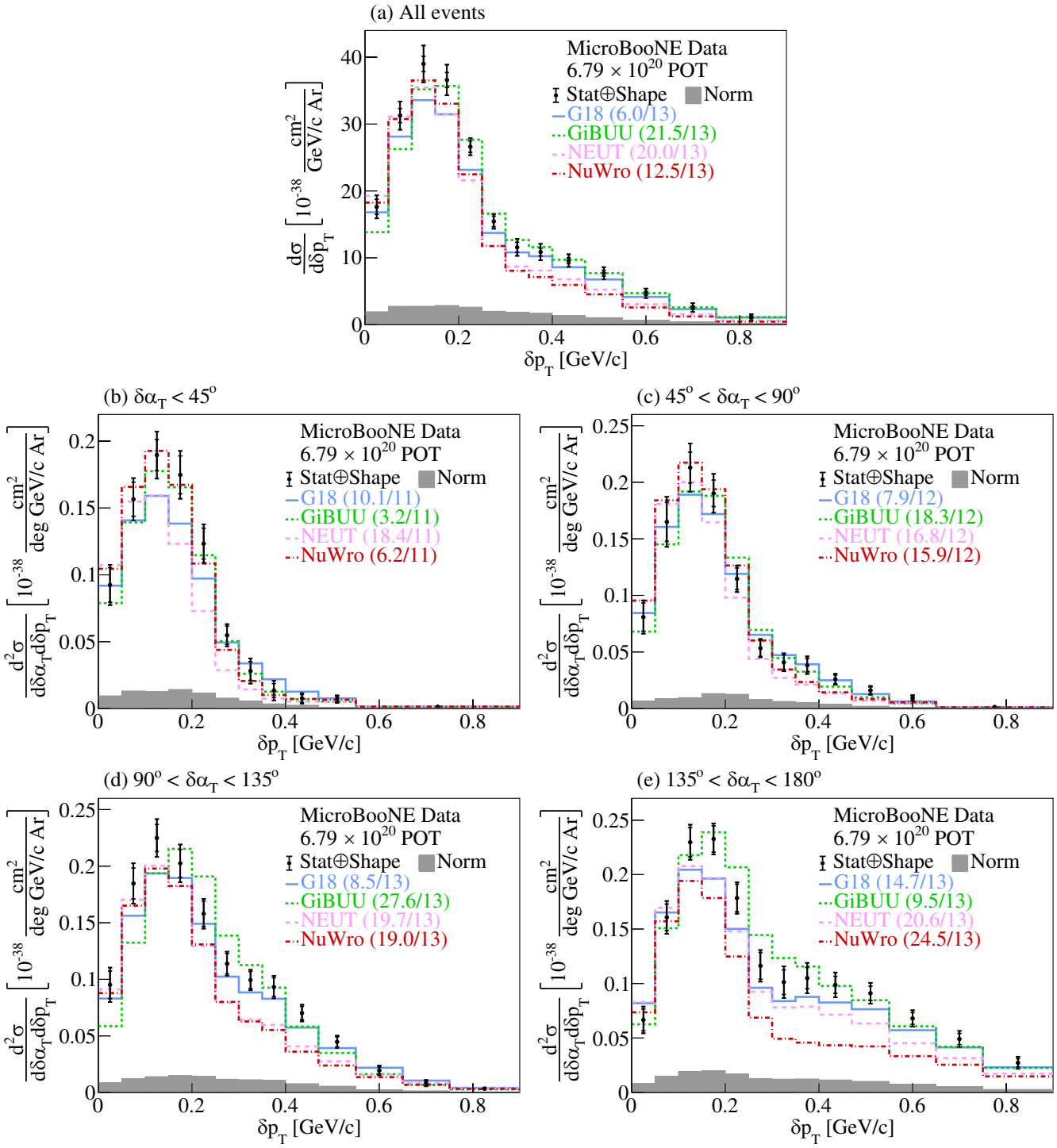

FIG. 12. The flux-integrated (a) single- and (b)–(e) double- (in $\delta\alpha_T$ bins) differential cross sections as a function of δp_T. Inner and outer error bars show the statistical and total (statistical and shape systematic) uncertainty at the 1σ, or 68%, confidence level. The gray band shows the normalization systematic uncertainty. Colored lines show the results of theoretical cross section calculations using the G18 GENIE (blue), GiBUU (green), NEUT (pink), and NuWro (red) event generators. The numbers in parentheses show the χ^2/bins calculation for each one of the predictions.

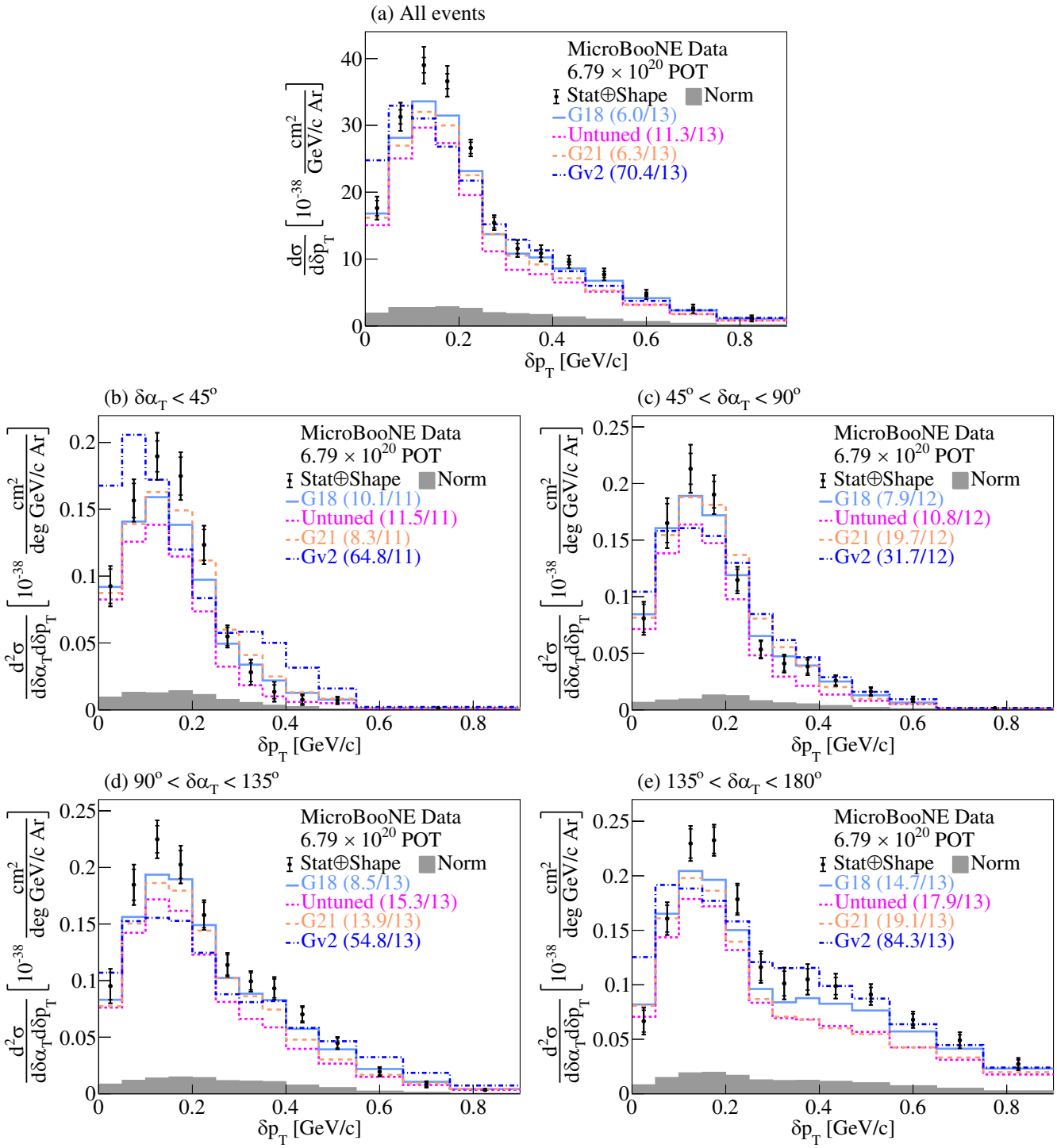

FIG. 13. The flux-integrated (a) single- and (b)–(e) double- (in $\delta\alpha_T$ bins) differential cross sections as a function of δp_T. Inner and outer error bars show the statistical and total (statistical and shape systematic) uncertainty at the 1σ, or 68%, confidence level. The gray band shows the normalization systematic uncertainty. Colored lines show the results of theoretical cross section calculations using the G18 (light blue), Untuned (magenta), G21 (orange), and Gv2 (dark blue) GENIE configurations. The numbers in parentheses show the χ^2/bins calculation for each one of the predictions.

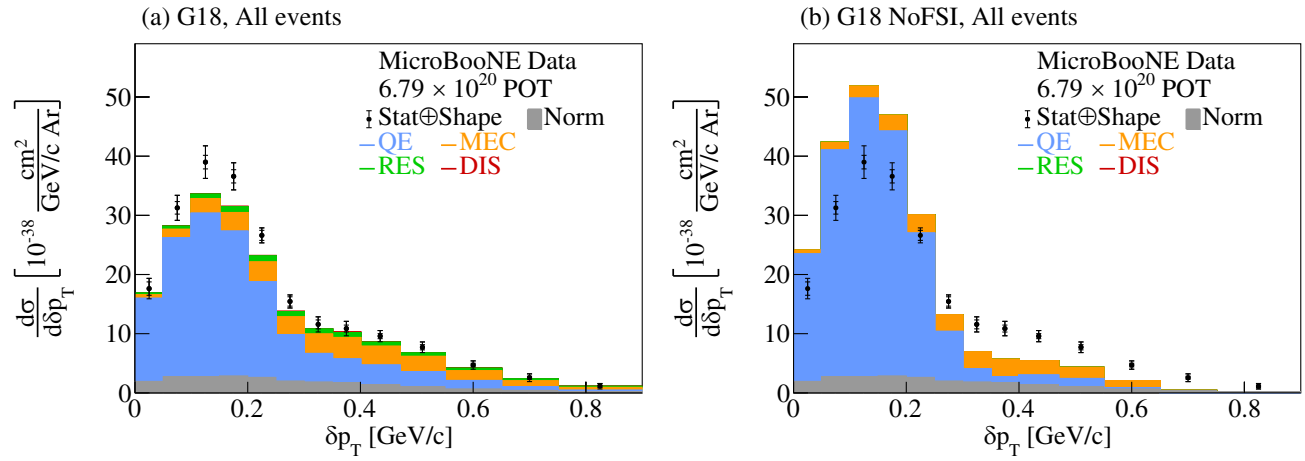

FIG. 14. Cross section interaction breakdown for the selected events for the G18 configuration (a) with FSI effects, and (b) without FSI effects as a function of δp_T.

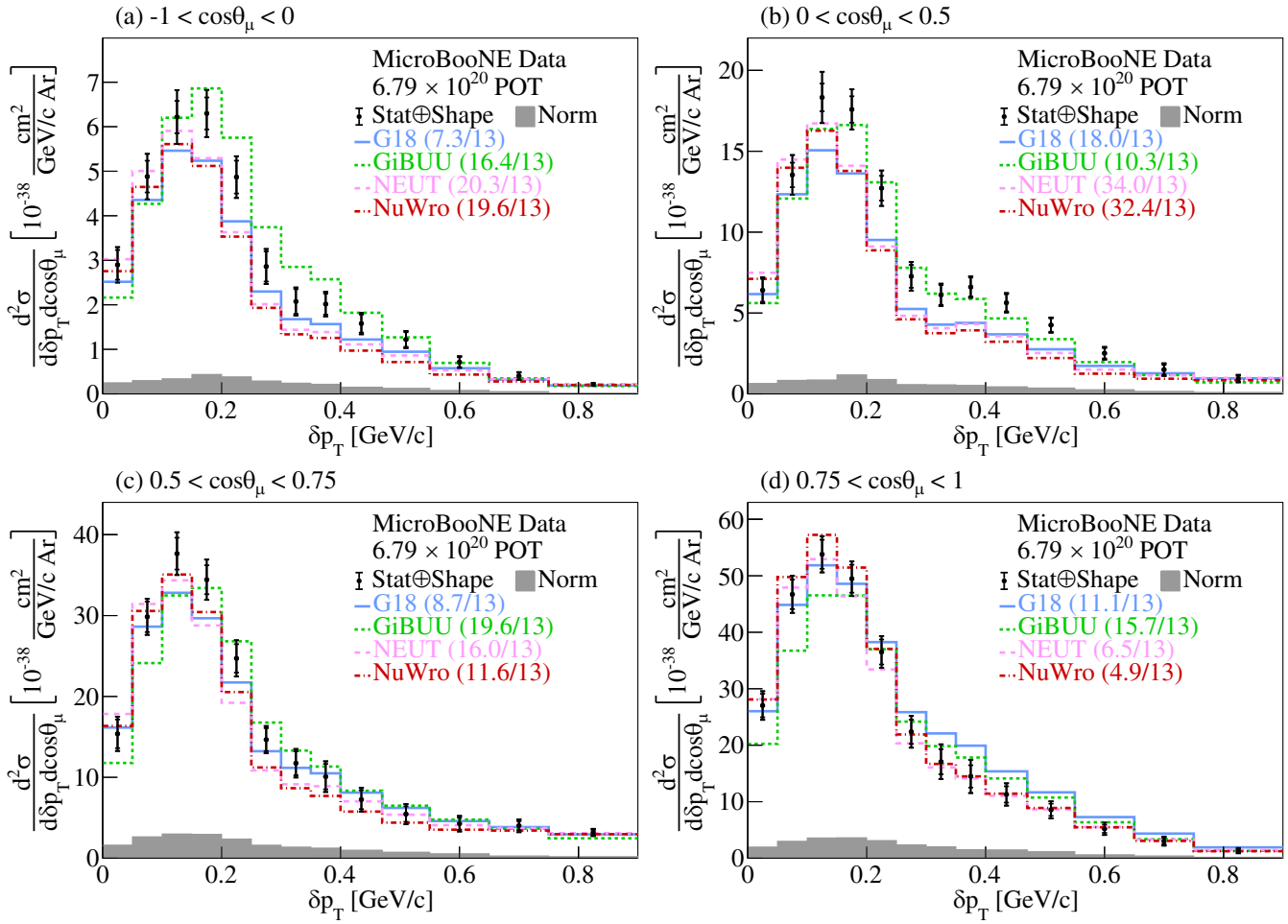

FIG. 15. The flux-integrated double-differential cross sections as a function of δp_T in $\cos\theta_\mu$ bins. Inner and outer error bars show the statistical and total (statistical and shape systematic) uncertainty at the 1σ, or 68%, confidence level. The gray band shows the normalization systematic uncertainty. Colored lines show the results of theoretical cross section calculations using the G18 GENIE (blue), GiBUU (green), NEUT (pink), and NuWro (red) event generators. The numbers in parentheses show the χ^2/bins calculation for each one of the predictions.

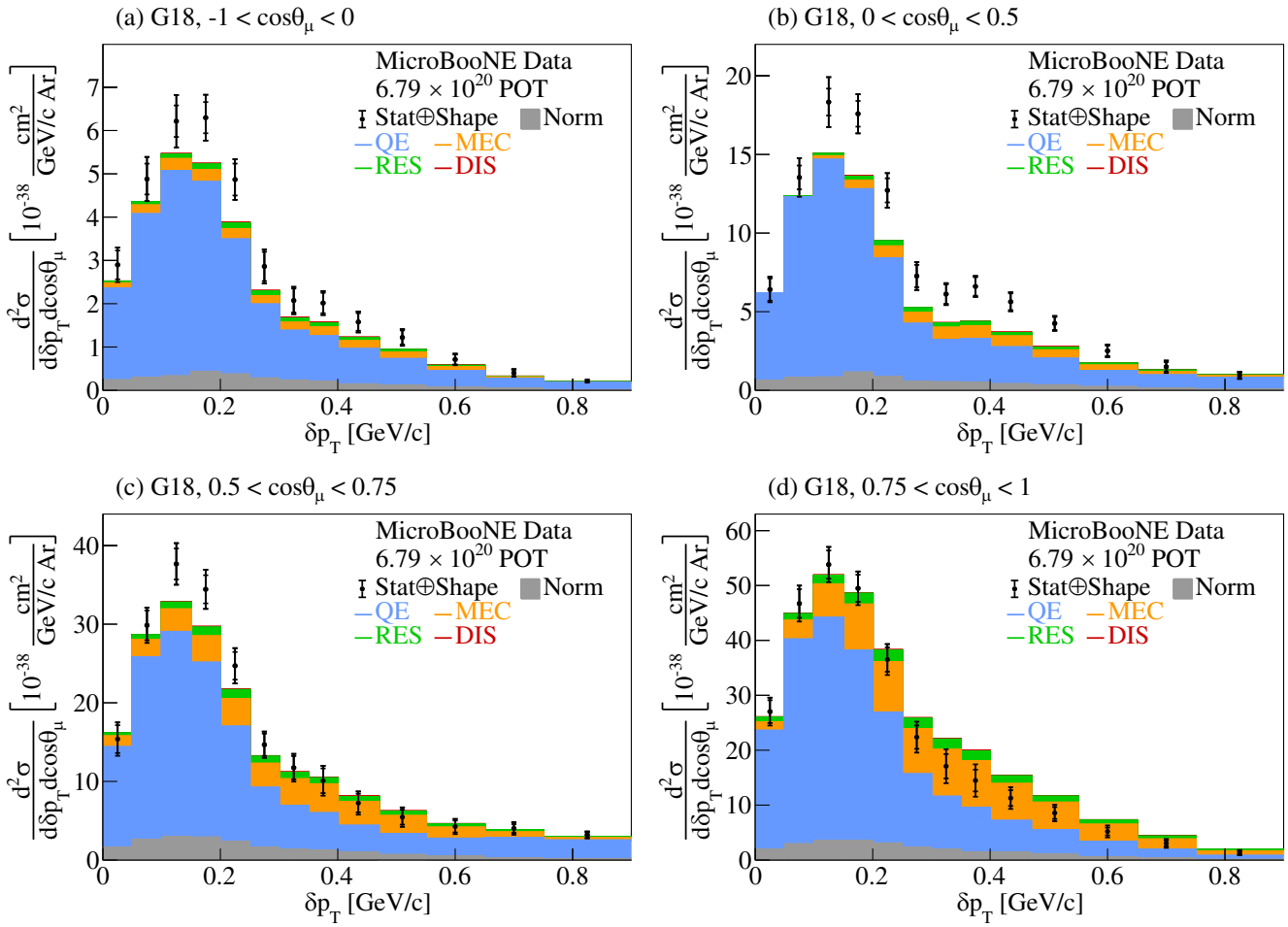

FIG. 16. Comparison between the flux-integrated double-differential cross sections as a function of δp_T for data and the G18 GENIE prediction in $\cos\theta_\mu$ bins. Inner and outer error bars show the statistical and total (statistical and shape systematic) uncertainty at the 1σ, or 68%, confidence level. The gray band shows the normalization systematic uncertainty. Colored stacked histograms show the results of theoretical cross section calculations using the GENIE prediction for QE (blue), MEC (orange), RES (green), and DIS (red) interactions.

($0.5 < \cos\theta_p < 1$), the Gv2 QE prediction yields a pronounced contribution at lower values of δp_T compared to the data.

Figures 22 and 23 show the single-differential cross sections as a function of $\delta\alpha_T$ using all the events [panel (a)], as well as the double-differential results in the same kinematic variable in δp_T bins [panels (b)–(d)]. The single-differential results shown in (a) yield some interesting observations when compared to the relevant T2K and MINERvA results [14,15,73]. Our distribution illustrates a slightly asymmetric behavior, similar to the one reported by the T2K Collaboration at a comparable energy with MicroBooNE. Both the already-published T2K results on carbon and the ones presented in this work on argon mostly demonstrate data-MC agreement within the experimental uncertainties. Therefore, the mass-number dependence of the nuclear effects seems to be reasonably well modeled. Unlike our result, the measurement by MINERvA reports a more pronounced asymmetry on hydrocarbon. The breakdown plots in Fig. 18 in Ref. [73] show that this behavior is driven by enhanced pion-production rates due to the higher average beam energy. Low δp_T values result in a fairly uniform $\delta\alpha_T$ distribution indicative of the absence of FSI effects in that part of the phase space. On the other hand, higher δp_T values result in a highly asymmetric $\delta\alpha_T$ distribution, which is driven by the strength of the FSI interactions. Figure 22 shows the comparisons to a number of available neutrino event generators, where NuWro is the generator with the most conservative FSI strength. Figure 23 shows the same results compared to a number of GENIE configurations, where Gv2 yields the highest χ^2/bins result, especially in the lowest δp_T region. As shown in Fig. 24, this is driven by the Gv2 QE performance, which results in peaks at the edges of the distribution, unlike the data result. Additionally, Fig. 25 shows the effect of FSI on the CC1p0π selection using the G18 configuration of GENIE that introduces an asymmetric behavior in $\delta\alpha_T$.

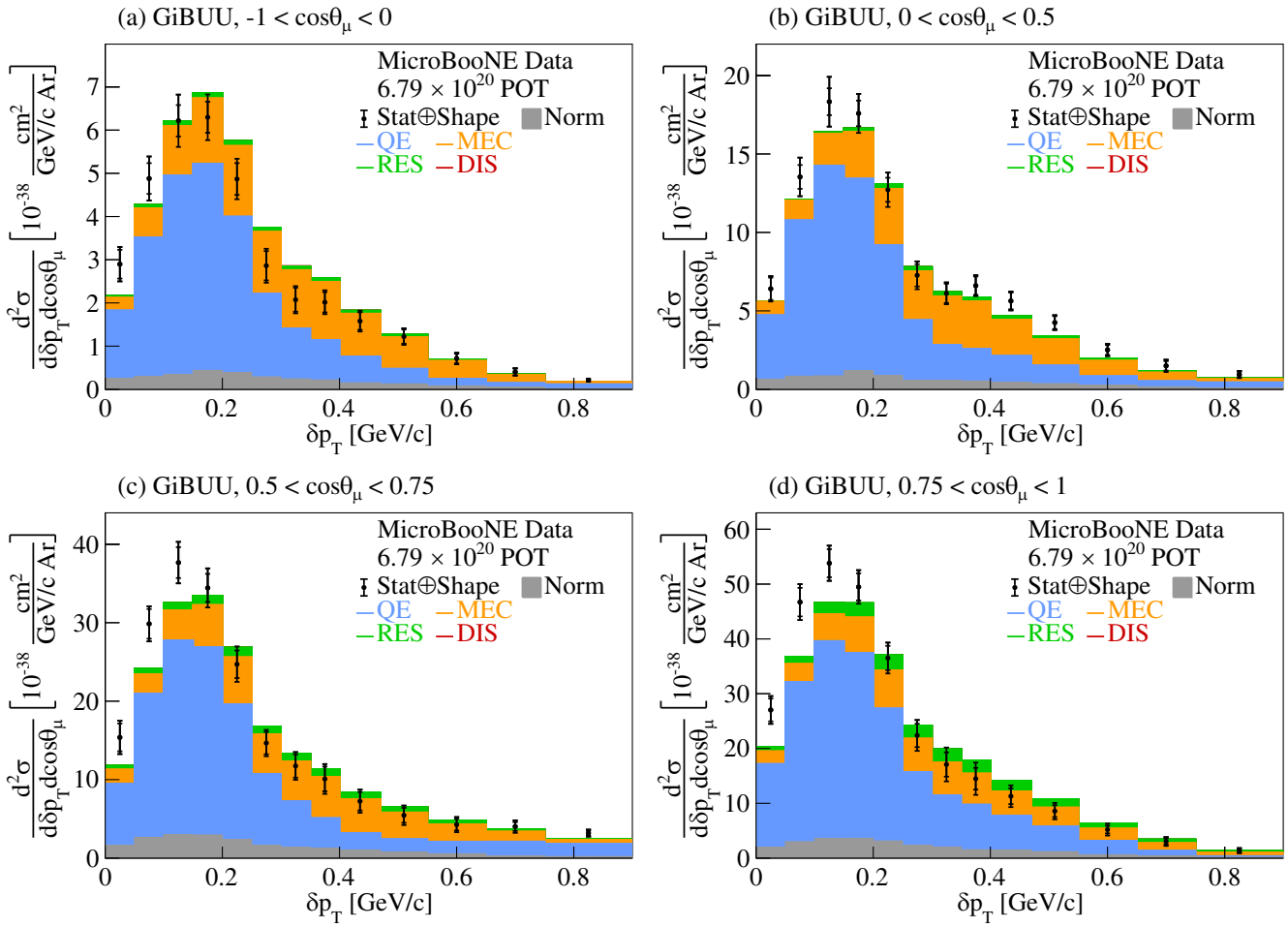

FIG. 17. Comparison between the flux-integrated double-differential cross sections as a function of δp_T for data and the GiBUU prediction in $\cos\theta_\mu$ bins. Inner and outer error bars show the statistical and total (statistical and shape systematic) uncertainty at the 1σ, or 68%, confidence level. The gray band shows the normalization systematic uncertainty. Colored stacked histograms show the results of theoretical cross section calculations using the GiBUU prediction for QE (blue), MEC (orange), RES (green), and DIS (red) interactions.

Figures 26 and 27 show the double-differential results as a function of $\delta\alpha_T$ in $\cos\theta_\mu$ bins. All the bins illustrate an asymmetric $\delta\alpha_T$ distribution, with the exception of the region where $\cos\theta_\mu \approx 1$, with the latter implying that this part of phase space includes events with minimal FSI effects. Figure 26 shows the comparisons to a number of available neutrino event generators with GiBUU giving the best performance. Figure 27 shows the same results compared to a number of GENIE configurations, illustrating that Gv2 is disfavored in the region where $\cos\theta_\mu < 0.75$.

Figures 28 and 29 show the double-differential cross sections as a function of $\delta\alpha_T$ in $\cos\theta_p$ bins. The results in the region with $0 < \cos\theta_p < 0.75$ show a fairly flat distribution. The cross section distributions corresponding to forward and backward proton scattering exhibit an FSI-driven asymmetric behavior. Figure 28 shows the comparisons to a number of available neutrino event generators, where NuWro yields a prediction that is disfavored for forward scattering. Figure 29 shows the same results compared to a number of GENIE configurations, illustrating that Gv2 is disfavored across all $\cos\theta_p$ bins. In the $-1 < \cos\theta_p < 0$ region shown in Fig. 29(a), all the predictions illustrate a peak close to 180° with the exception of Gv2. The driving force for this difference is the Gv2 QE contribution, as can be seen in Fig. 30. This is indicative of potential modeling issues in the Llewellyn Smith QE cross section and of the hA FSI performance used in the Gv2 prediction. Unlike Gv2, the theory-driven GENIE v3 family of predictions (G18, Untuned, and G21) closely follow the data.

Figures 31 and 32 show the single-differential cross sections as a function of $\delta\phi_T$ using all the events [panel (a)], as well as the double-differential results as a function of the same kinematic variable in δp_T bins [panels (b)–(d)]. Figure 31 shows the comparisons to a number of available neutrino event generators, with all the generators illustrating a fairly good performance. This result is consistent with the one reported by the T2K Collaboration [14,73].

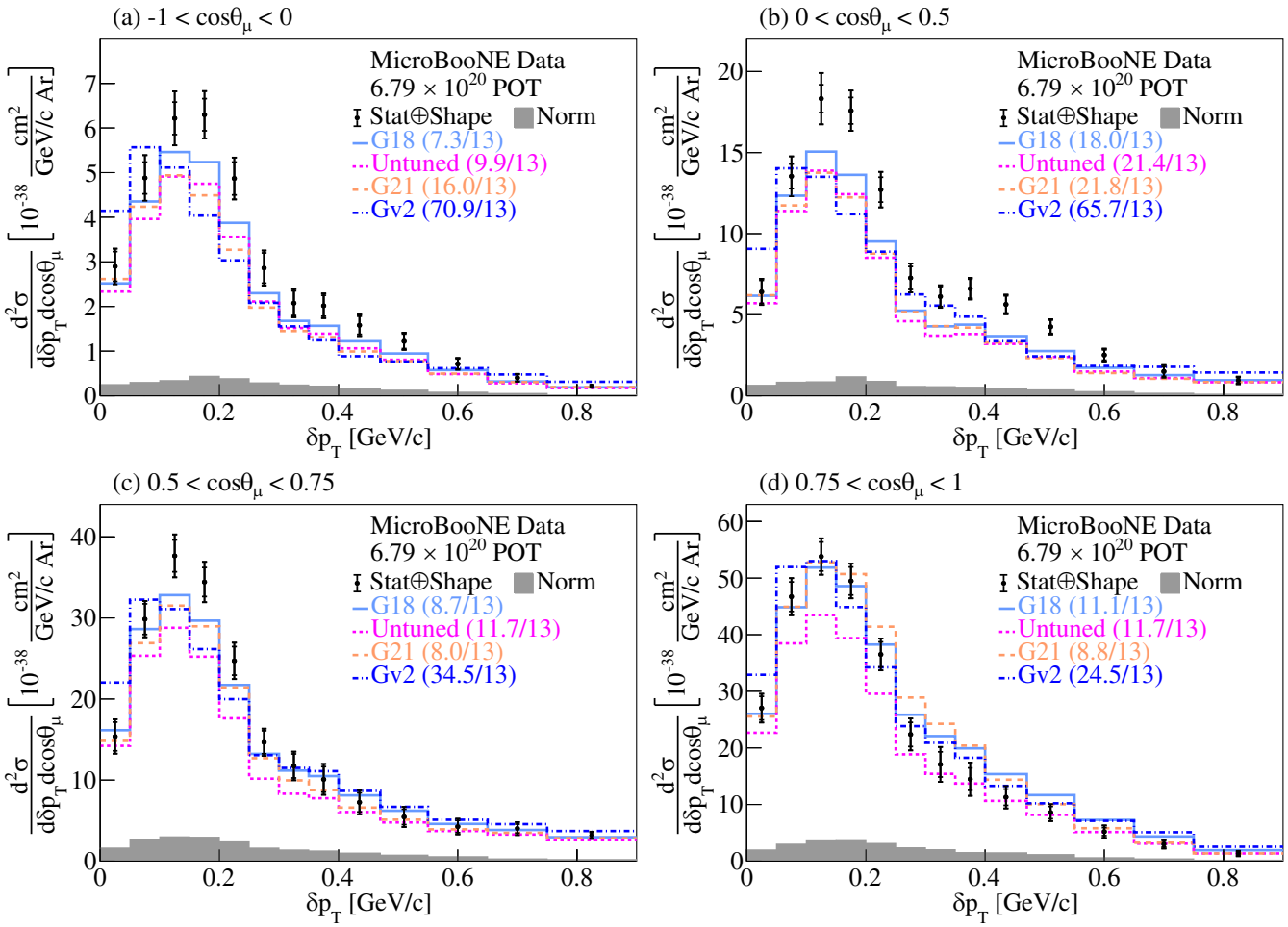

FIG. 18. The flux-integrated double-differential cross sections as a function of δp_T in $\cos\theta_\mu$ bins. Inner and outer error bars show the statistical and total (statistical and shape systematic) uncertainty at the 1σ, or 68%, confidence level. The gray band shows the normalization systematic uncertainty. Colored lines show the results of theoretical cross section calculations using the G18 (light blue), Untuned (magenta), G21 (orange), and Gv2 (dark blue) GENIE configurations. The numbers in parentheses show the χ^2/bins calculation for each one of the predictions.

In the lowest δp_T region shown in panel (b), NuWro is the generator with the best performance. Figure 32 shows the same results compared to a number of GENIE configurations, where Gv2 is disfavored in all regions. At small δp_T values the cross section is decreasing and zero above ≈40° which indicates the absence of multinucleon and FSI effects. Higher δp_T values lead to $\delta\phi_T$ cross sections that extend up to 180°. This behavior is primarily driven by multibody effects with hadrons below the detection threshold that introduce large kinematic imbalances, as can be seen in panels (c)–(d) of Fig. 33.

Figures 34 and 35 show the single-differential cross sections as a function of $\delta p_{T,x}$ using all the events [panel (a)], as well as the double-differential results in the same kinematic variable in $\delta p_{T,y}$ slices [panels (b)–(c)]. Figure 34 shows the comparisons to a number of available neutrino event generators. The central region with $|\delta p_{T,y}| < 0.15$ GeV/c is dominated by QE interactions, while the broader distributions with $|\delta p_{T,y}| > 0.15$ GeV/c are mainly driven by MEC events, as can be seen in Fig. 36. In the MEC dominated region of $\delta p_{T,y} < -0.15$ GeV/c, all the generators, apart from GiBUU, seem to be lacking in terms of the peak strength. GiBUU seems to be overestimating that MEC contribution in the $\delta p_{T,y} < -0.15$ GeV/c bin. With the exception of NEUT, all the event generators illustrate a good performance in the $|\delta p_{T,y}| < 0.15$ GeV/c region. Figure 35 shows the same results compared to a number of GENIE configurations, where Gv2 shows the worst performance.

The aforementioned results in kinematic imbalance variables illustrate significant differences across the event generators and configurations used for comparison, especially in the case of the double-differential studies. Yet, the quantity that enters the oscillation probability is the true neutrino energy. Neutrino energy estimators, such as the calorimetric energy E^{Cal} defined in Eq. (6), are used as a

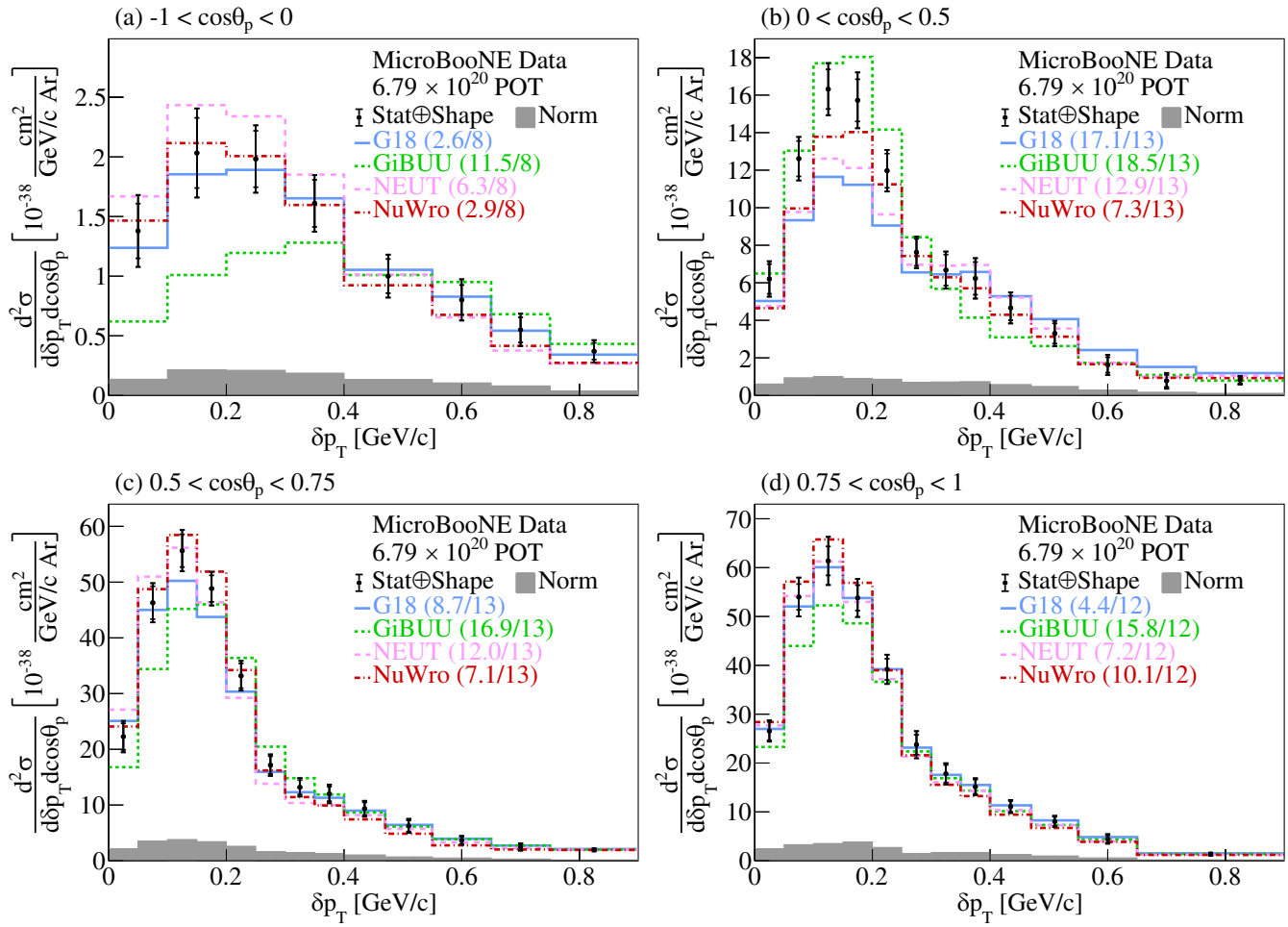

FIG. 19. The flux-integrated double-differential cross sections as a function of δp_T in $\cos\theta_p$ bins. Inner and outer error bars show the statistical and total (statistical and shape systematic) uncertainty at the 1σ, or 68%, confidence level. The gray band shows the normalization systematic uncertainty. Colored lines show the results of theoretical cross section calculations using the G18 GENIE (blue), GiBUU (green), NEUT (pink), and NuWro (red) event generators. The numbers in parentheses show the χ^2/bins calculation for each one of the predictions.

proxy for the true quantity. The studies reported next present the results as a function of E^{Cal} in bins of the kinematic imbalance variables.

Figures 37 and 38 show the single-differential cross sections as a function of E^{Cal} using all the events [panel (a)], as well as the double-differential results in the same kinematic variable in δp_T bins [panels (b)–(d)]. Figure 37 shows the comparisons to a number of available neutrino event generators, where the E^{Cal} distribution covers the same energy spectrum across all bins. All the event generators illustrate an equally good performance in the lowest δp_T bin. NEUT and NuWro show a deficit relative to the data in the highest δp_T bins. Figure 38 shows the same results compared to a number of GENIE configurations, where G18 illustrates the best performance. In the lowest δp_T bin, the different configurations illustrate a shift to the left compared to the data, unlike G18, which drives the significantly higher χ^2 values. Interestingly, all the alternative GENIE configurations illustrate a plateau in the highest δp_T bin that also yields high χ^2/bins ratios.

Figures 39 and 40 show the double-differential results as a function of E^{Cal} in $\delta\alpha_T$ bins. Figure 39 shows the comparisons to a number of available neutrino event generators. Once again, the E^{Cal} distribution covers the same energy spectrum across all of our results, and all the event generators show fairly good behavior. NuWro illustrates a mild deficit in the $135° < \delta\alpha_T < 180°$ bin, which is also reflected in the χ^2/bins ratio. Figure 40 shows the same results compared to a number of GENIE configurations, where all the GENIE configurations except for G18 illustrate shape and strength differences.

Figures 41 and 42 show the double-differential results as a function of E^{Cal} in $\delta p_{T,y}$ bins. Figure 41 shows the comparisons to a number of available neutrino event generators. All event generators predict very similar cross sections for $-0.15 < \delta p_{T,y} < 0.15$ GeV/c [panel (a)].

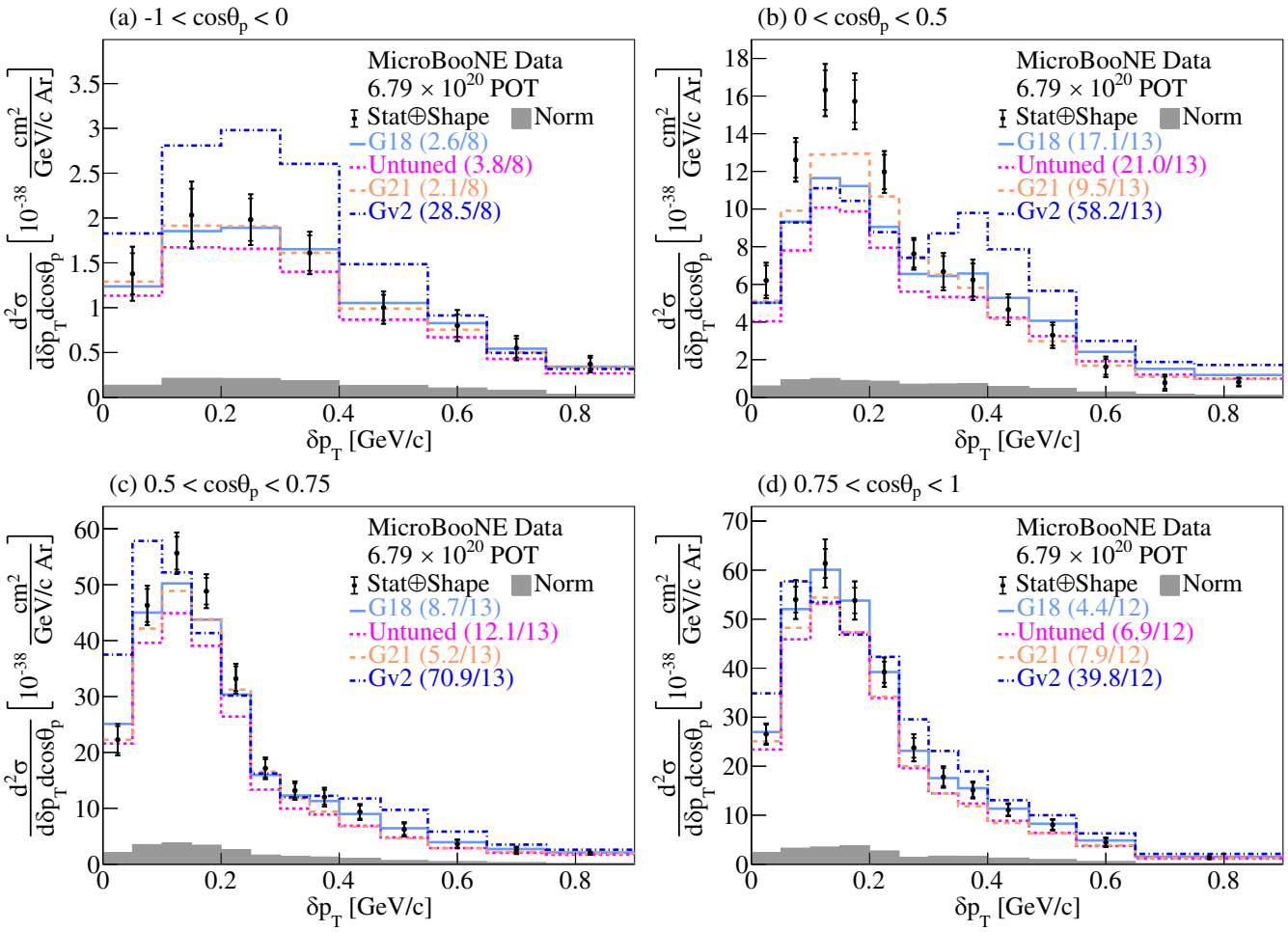

FIG. 20. The flux-integrated double-differential cross sections as a function of δp_T in $\cos\theta_p$ bins. Inner and outer error bars show the statistical and total (statistical and shape systematic) uncertainty at the 1σ, or 68%, confidence level. The gray band shows the normalization systematic uncertainty. Colored lines show the results of theoretical cross section calculations using the G18 (light blue), Untuned (magenta), G21 (orange), and Gv2 (dark blue) GENIE configurations. The numbers in parentheses show the χ^2/bins calculation for each one of the predictions.

Unlike this central region, the $|\delta p_{T,y}| > 0.15$ GeV/c results yield a wide spread across the generator predictions [panels (b)–(c)]. Furthermore, apart from GiBUU, all the predictions lack strength in the $\delta p_{T,y} < -0.15$ GeV/c bin [panel (b)]. Additionally, NEUT illustrates the same deficit in the $\delta p_{T,y} > 0.15$ GeV/c bin [panel (c)]. Figure 42 shows the same results compared to a number of GENIE configurations, where all the GENIE configurations but G18 illustrate a poor performance due to shape and strength issues.

VIII. CONCLUSIONS

This work reports on measurements of flux-integrated differential cross sections for event topologies with a single muon and a single proton detected in the final state using the Booster Neutrino Beam at the Fermi National Accelerator Laboratory and the MicroBooNE detector. The data were studied for the first time in the form of single-differential cross sections in kinematic imbalance variables on argon. Furthermore, the first double-differential cross sections in these variables were reported on the same nucleus. Additionally, novel double-differential cross section measurements of a neutrino energy estimator in bins of these variables were presented. The results were compared to a number of event generators and model configurations. The predictions as a function of the energy estimator across all generators and model configurations remain mostly unchanged regardless of the kinematic variable used for the double-differential measurements. Based on the reported χ^2/bins, the good agreement observed across the calorimetric energy distributions suggests that the energy dependence is largely well modeled across most predictions. Unlike the energy estimator results, we found that the measured kinematic imbalance cross sections in different phase-space regions are sensitive to nuclear effects. The performance of the event generators and configurations varies depending

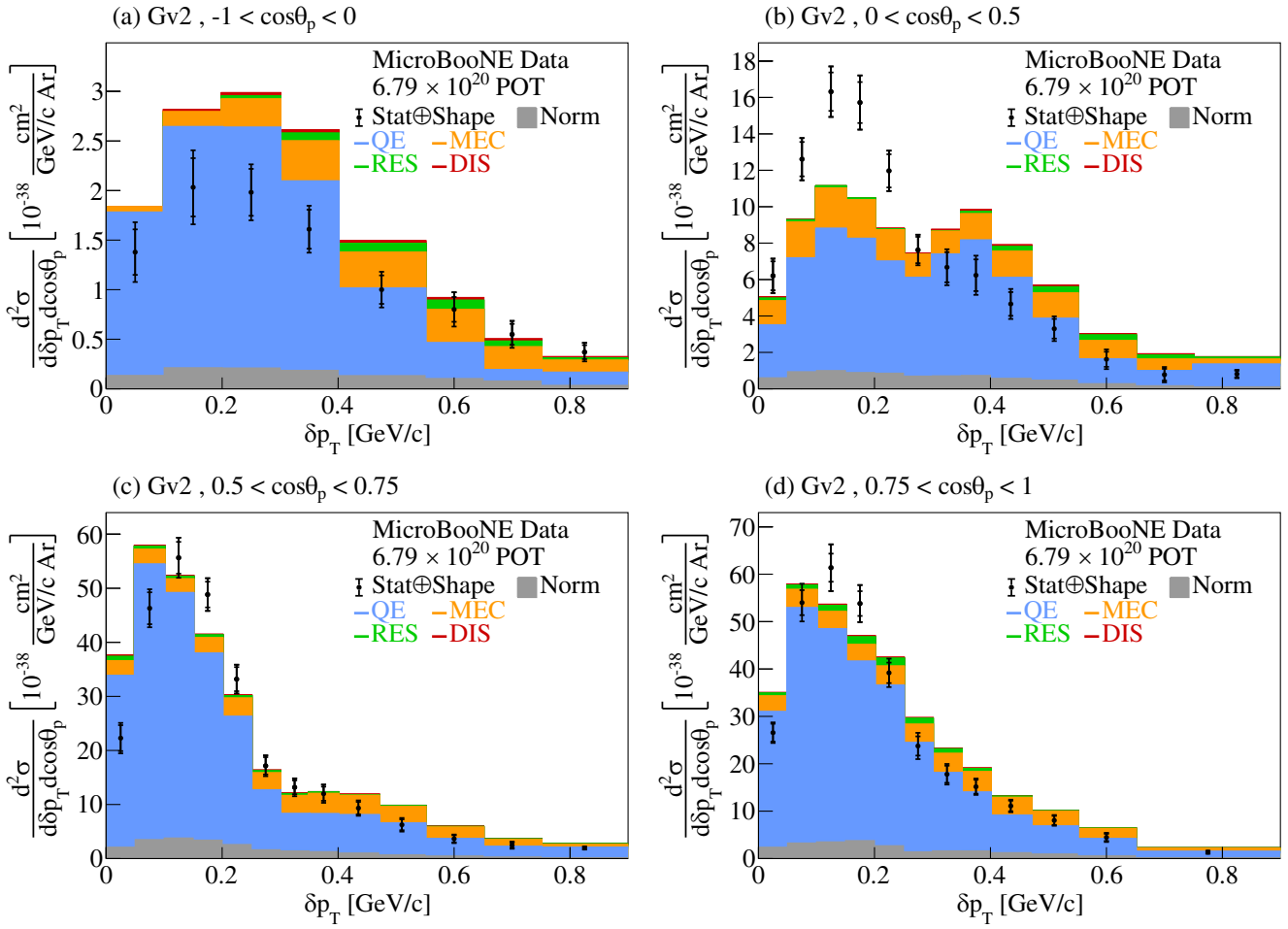

FIG. 21. Comparison between the flux-integrated double-differential cross sections as a function of δp_T for data and the Gv2 GENIE prediction in $\cos\theta_p$ bins. Inner and outer error bars show the statistical and total (statistical and shape systematic) uncertainty at the 1σ, or 68%, confidence level. The gray band shows the normalization systematic uncertainty. Colored stacked histograms show the results of theoretical cross section calculations using the GENIE prediction for QE (blue), MEC (orange), RES (green), and DIS (red) interactions.

on the observable of interest. Overall, the GENIE v3.0.6 G18_10a_02_11a cross section predictions with the MicroBooNE-specific tuning (G18) fit the data well. On the other hand, the GENIE v2.12.10 (Gv2) cross section predictions are systematically a poor fit to data with significant shape differences across all variables of interest. The GENIE v3.0.6 G18_10a_02_11a configuration without additional tuning (Untuned) shows a systematic deficit of ~20% which necessitated the development of the aforementioned tune. The GENIE v3.2.0 G21_11b_00_000 configuration (G21) serves as an example of a theory-driven GENIE configuration that shows good agreement with data in most variables without the need for additional tuning. GiBUU 2021 (GiBUU) shows good agreement with data in most kinematic variables, with the exception of δp_T, where a systematic shift to higher values of δp_T has been identified. A potential source of this shift is due to the GiBUU MEC modeling. The NuWro v19.02.2 (NuWro) prediction falls below the data due to poor FSI modeling and shows significant shape differences in FSI-dominated parts of the phase space. NEUT v5.4.0 (NEUT) also results in predictions mostly falling below the data points. This mismodeling remains largely unnoticed when combined into the calorimetric energy estimator. Yet, future neutrino oscillation measurements will rely on accurate cross section predictions and a precise mapping between measured and true neutrino energies. Therefore, such mismodeling effects might impact their experimental sensitivity. The reported results both provide precision data to benchmark neutrino-nucleus interaction models and establish phase-space regions where precise reaction modeling is still needed.

ACKNOWLEDGMENTS

This document was prepared by the MicroBooNE Collaboration using the resources of the Fermi National Accelerator Laboratory (Fermilab), a U.S. Department of Energy, Office of Science, HEP User Facility. Fermilab is managed by Fermi Research Alliance, LLC (FRA), acting under Contract No. DE-AC02-07CH11359. This material

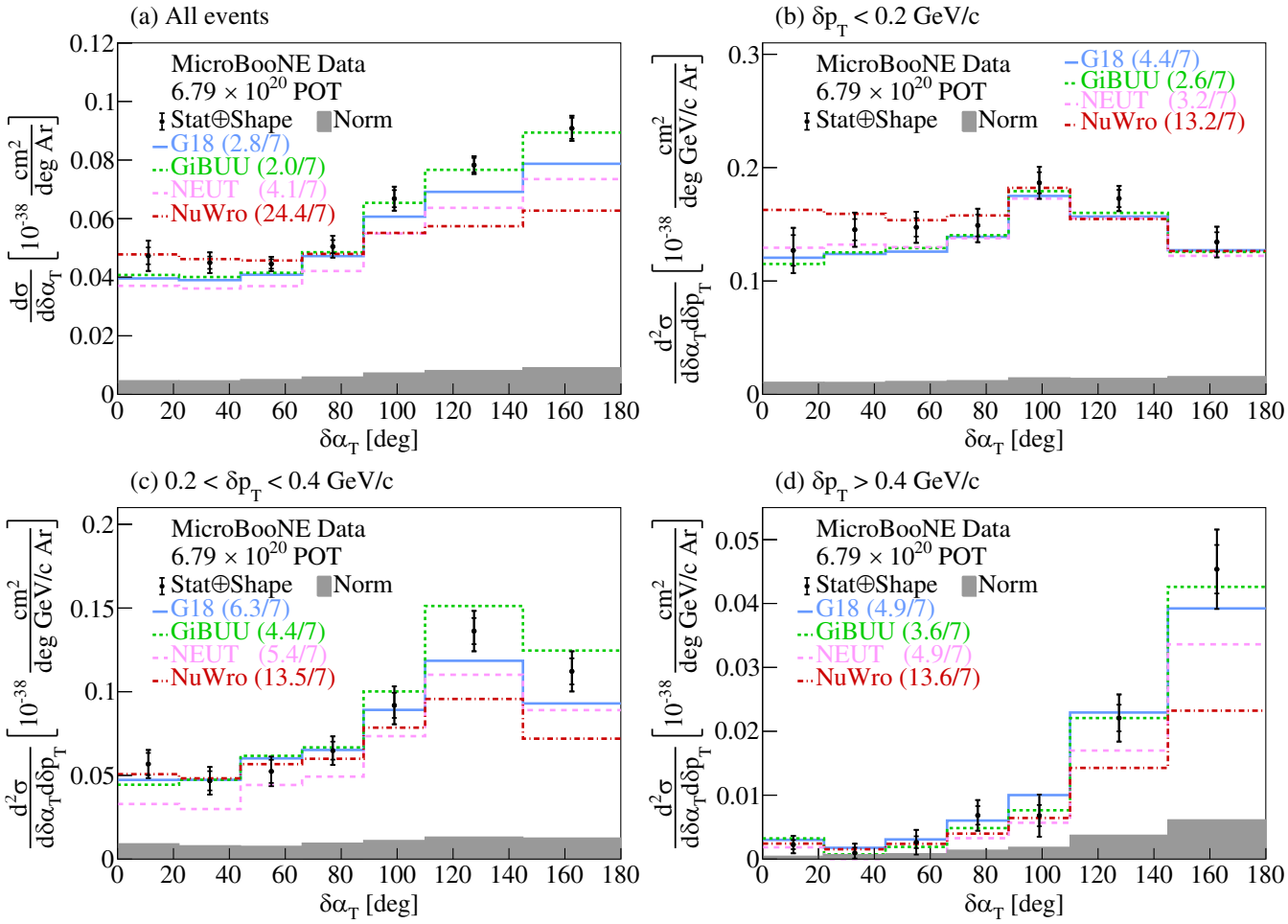

FIG. 22. The flux-integrated (a) single- and (b)–(d) double- (in δp_T bins) differential cross sections as a function of $\delta\alpha_T$. Inner and outer error bars show the statistical and total (statistical and shape systematic) uncertainty at the 1σ, or 68%, confidence level. The gray band shows the normalization systematic uncertainty. Colored lines show the results of theoretical cross section calculations using the G18 GENIE (blue), GiBUU (green), NEUT (pink), and NuWro (red) event generators. The numbers in parentheses show the χ^2/bins calculation for each one of the predictions.

is based upon work supported by Laboratory Directed Research and Development (LDRD) funding from Argonne National Laboratory, provided by the Director, Office of Science, of the U.S. Department of Energy under Contract No. DE-AC02-06CH11357. MicroBooNE is supported by the following: the U.S. Department of Energy, Office of Science, Offices of High Energy Physics and Nuclear Physics; the U.S. National Science Foundation; the Swiss National Science Foundation; the Science and Technology Facilities Council (STFC), part of the United Kingdom Research and Innovation; the Royal Society (United Kingdom); the UK Research and Innovation (UKRI) Future Leaders Fellowship; and the NSF AI Institute for Artificial Intelligence and Fundamental Interactions; and The European Union's Horizon 2020 Marie Sklodowska-Curie Actions. Additional support for the laser calibration system and cosmic ray tagger was provided by the Albert Einstein Center for Fundamental Physics, Bern, Switzerland. We also acknowledge the contributions of technical and scientific staff to the design, construction, and operation of the MicroBooNE detector as well as the contributions of past collaborators to the development of MicroBooNE analyses, without whom this work would not have been possible.

Note added.—The reported results both provide precision data to benchmark neutrino-nucleus interaction models and establish phase-space regions where precise reaction modeling is still needed. Further discussion on the modeling performance against the same results can be found in Ref. [74].

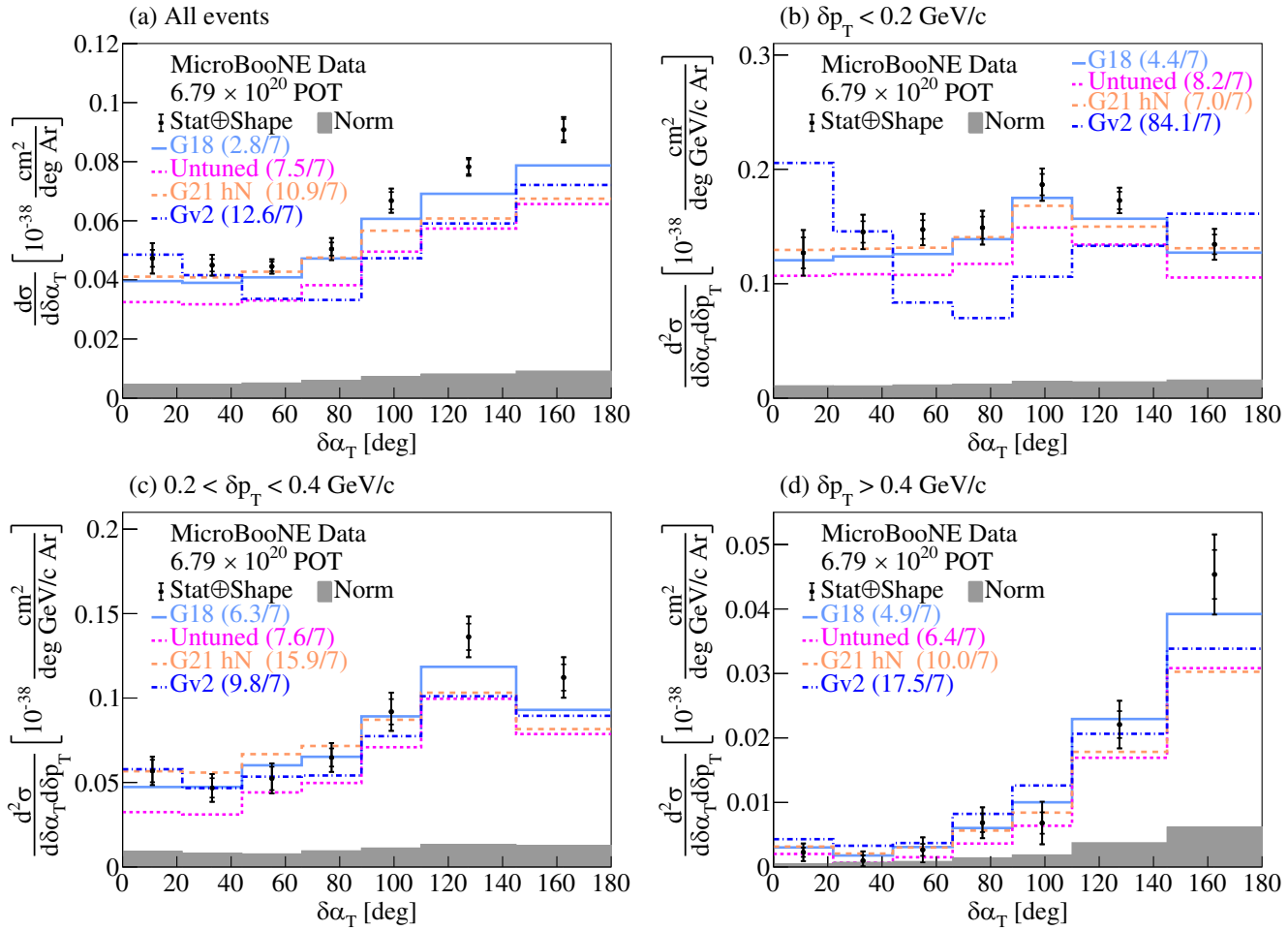

FIG. 23. The flux-integrated (a) single- and (b)–(d) double- (in δp_T bins) differential cross sections as a function of $\delta\alpha_T$. Inner and outer error bars show the statistical and total (statistical and shape systematic) uncertainty at the 1σ, or 68%, confidence level. The gray band shows the normalization systematic uncertainty. Colored lines show the results of theoretical cross section calculations using the G18 (light blue), Untuned (magenta), G21 (orange), and Gv2 (dark blue) GENIE configurations. The numbers in parentheses show the χ^2/bins calculation for each one of the predictions.

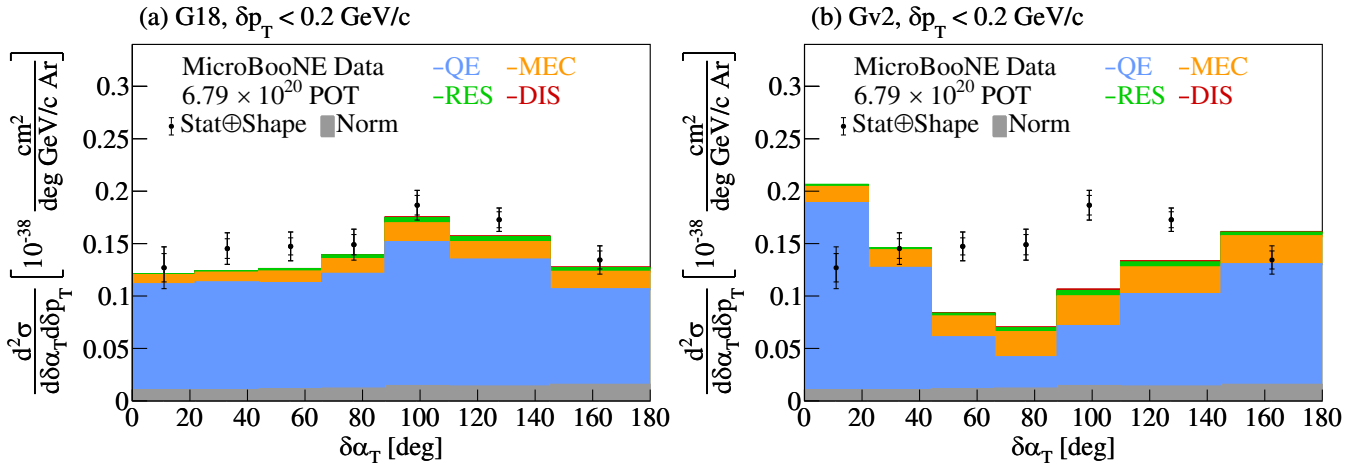

FIG. 24. Comparison between the data flux-integrated double-differential cross section as a function of $\delta\alpha_T$ for events in the region $\delta p_T < 0.2$ GeV/c region against the G18 and GENIE predictions. Inner and outer error bars show the statistical and total (statistical and shape systematic) uncertainty at the 1σ, or 68%, confidence level. The gray band shows the normalization systematic uncertainty. Colored stacked histograms show the results of theoretical cross section calculations using the (a) G18 and (b) Gv2 GENIE predictions for QE (blue), MEC (orange), RES (green), and DIS (red) interactions.

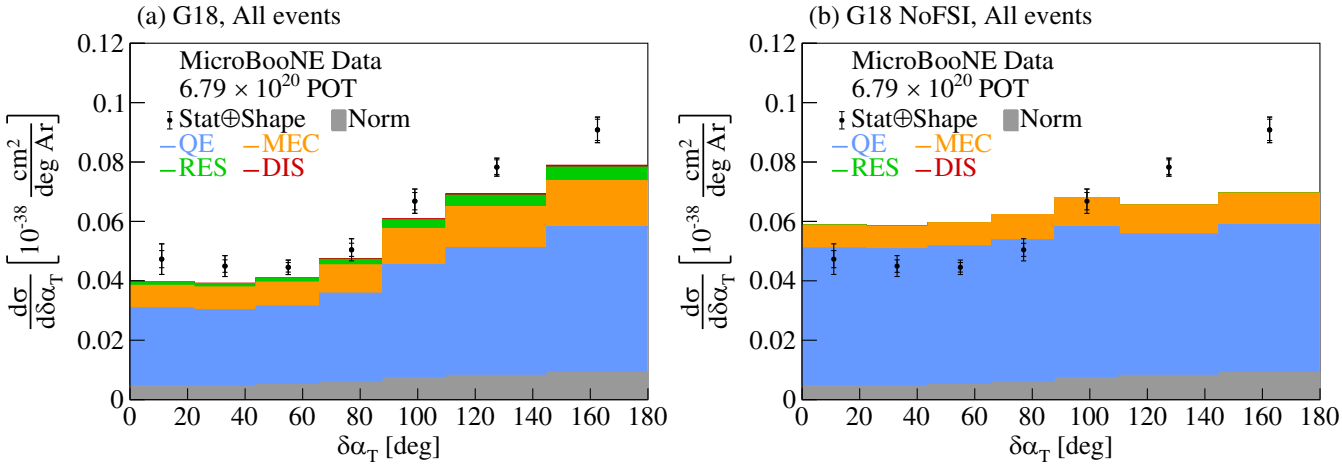

FIG. 25. Cross section interaction breakdown for the selected events for the G18 configuration (a) with FSI effects, and (b) without FSI effects as a function of $\delta\alpha_T$.

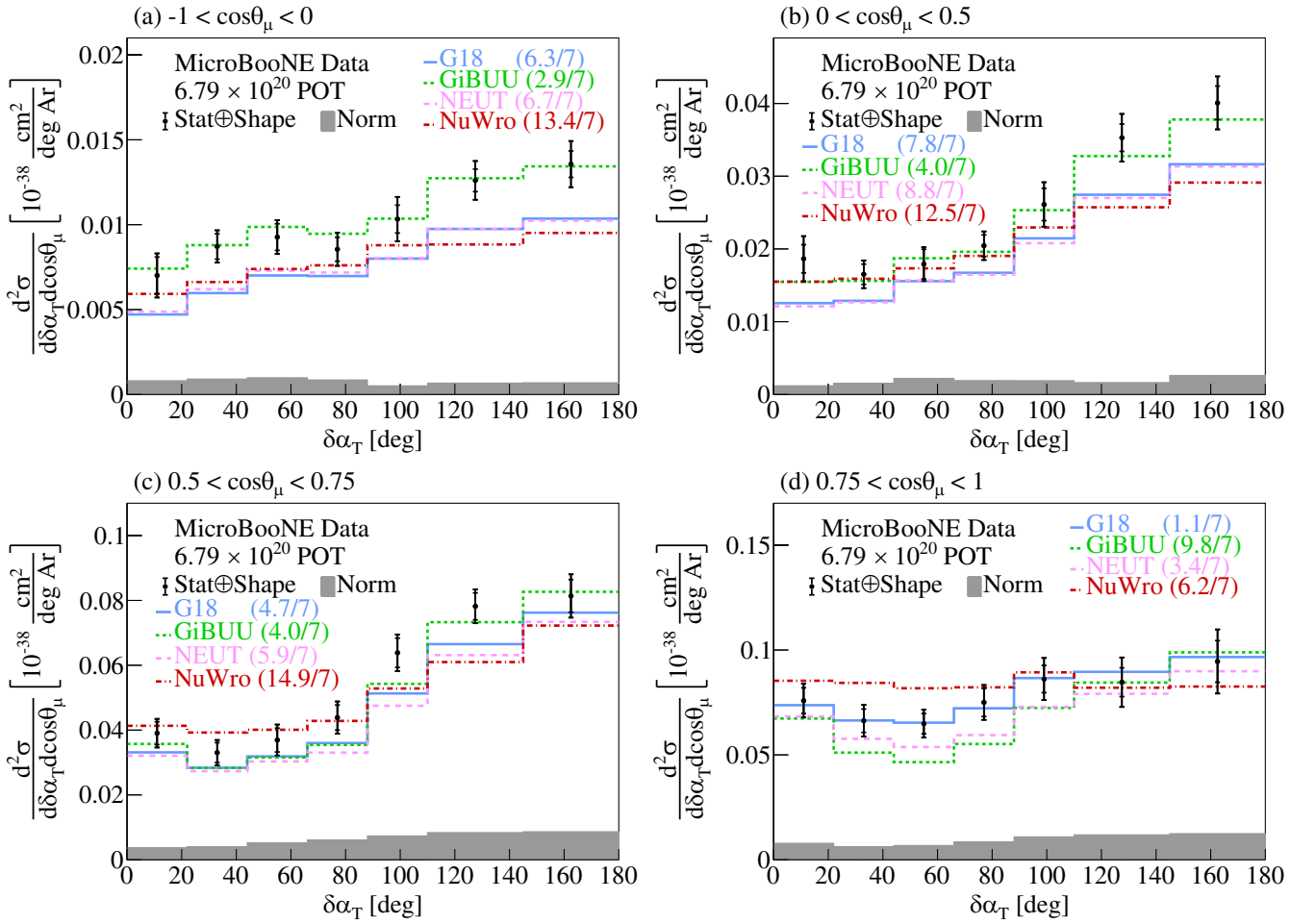

FIG. 26. The flux-integrated double-differential cross sections as a function of $\delta\alpha_T$ in $\cos\theta_\mu$ bins. Inner and outer error bars show the statistical and total (statistical and shape systematic) uncertainty at the 1σ, or 68%, confidence level. The gray band shows the normalization systematic uncertainty. Colored lines show the results of theoretical cross section calculations using the G18 GENIE (blue), GiBUU (green), NEUT (pink), and NuWro (red) event generators. The numbers in parentheses show the χ^2/bins calculation for each one of the predictions.

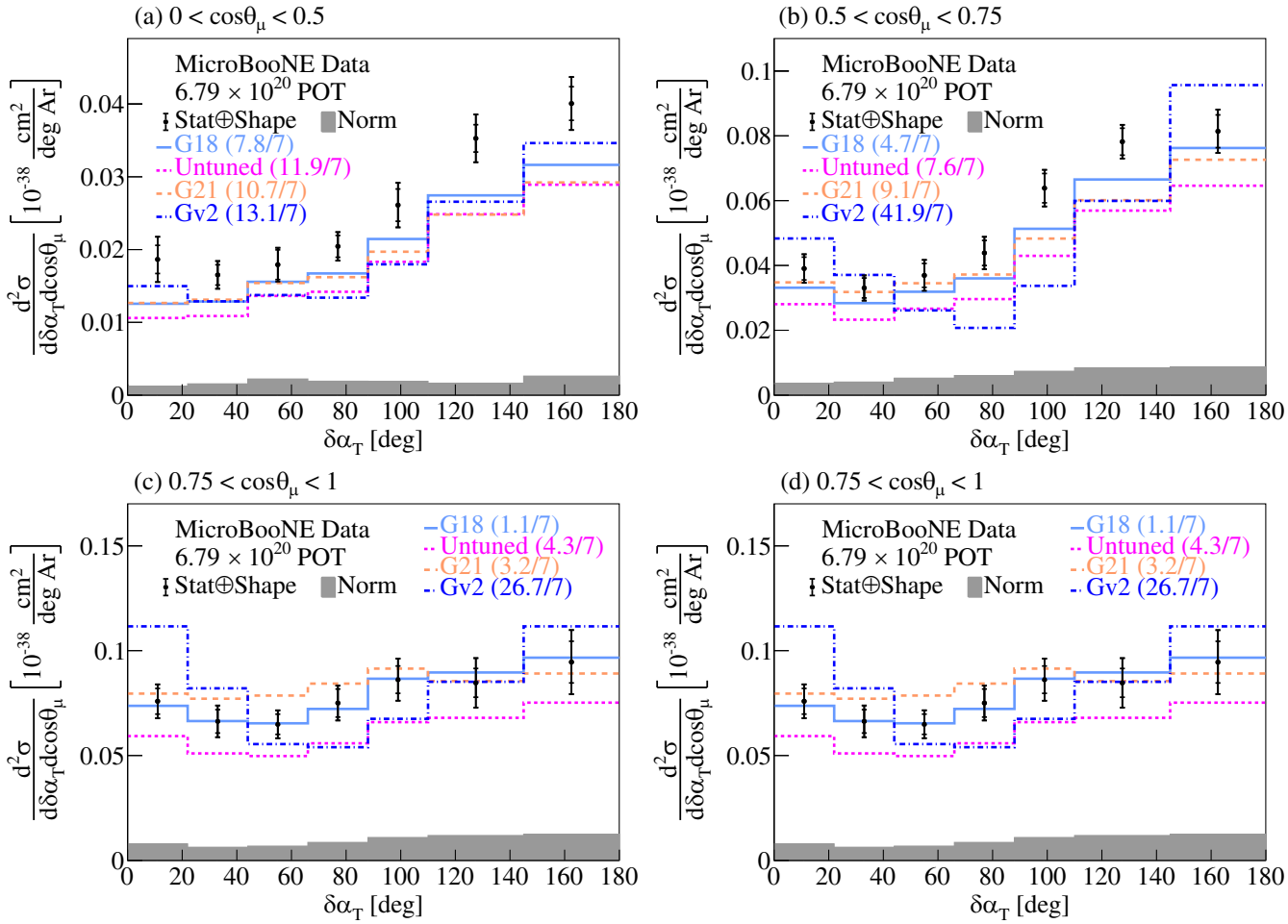

FIG. 27. The flux-integrated double-differential cross sections as a function of $\delta\alpha_T$ in $\cos\theta_\mu$ bins. Inner and outer error bars show the statistical and total (statistical and shape systematic) uncertainty at the 1σ, or 68%, confidence level. The gray band shows the normalization systematic uncertainty. Colored lines show the results of theoretical cross section calculations using the G18 (light blue), Untuned (magenta), G21 (orange), and Gv2 (dark blue) GENIE configurations. The numbers in parentheses show the χ^2/bins calculation for each one of the predictions.

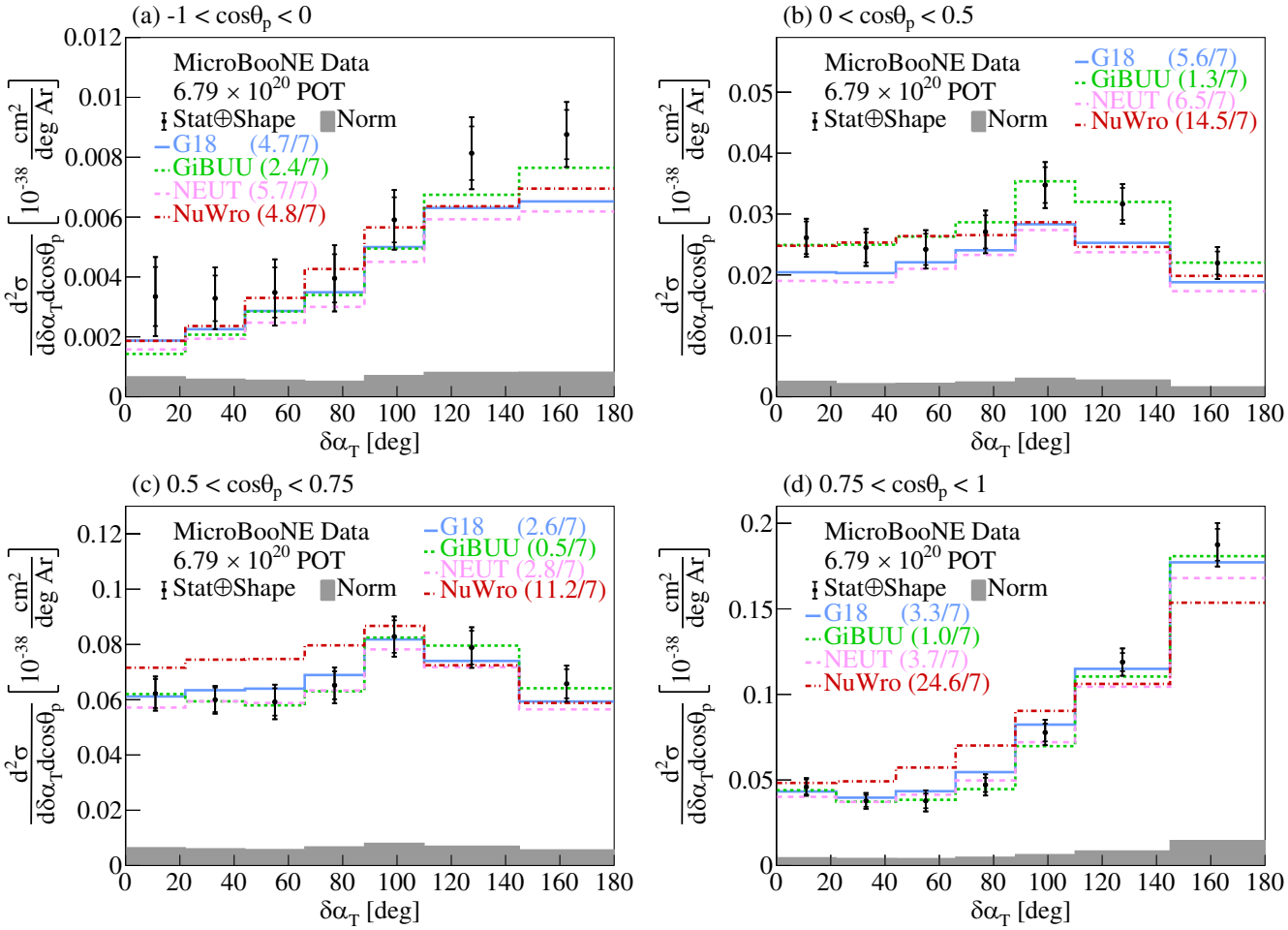

FIG. 28. The flux-integrated double-differential cross sections as a function of $\delta\alpha_T$ in $\cos\theta_p$ bins. Inner and outer error bars show the statistical and total (statistical and shape systematic) uncertainty at the 1σ, or 68%, confidence level. The gray band shows the normalization systematic uncertainty. Colored lines show the results of theoretical cross section calculations using the G18 GENIE (blue), GiBUU (green), NEUT (pink), and NuWro (red) event generators. The numbers in parentheses show the χ^2/bins calculation for each one of the predictions.

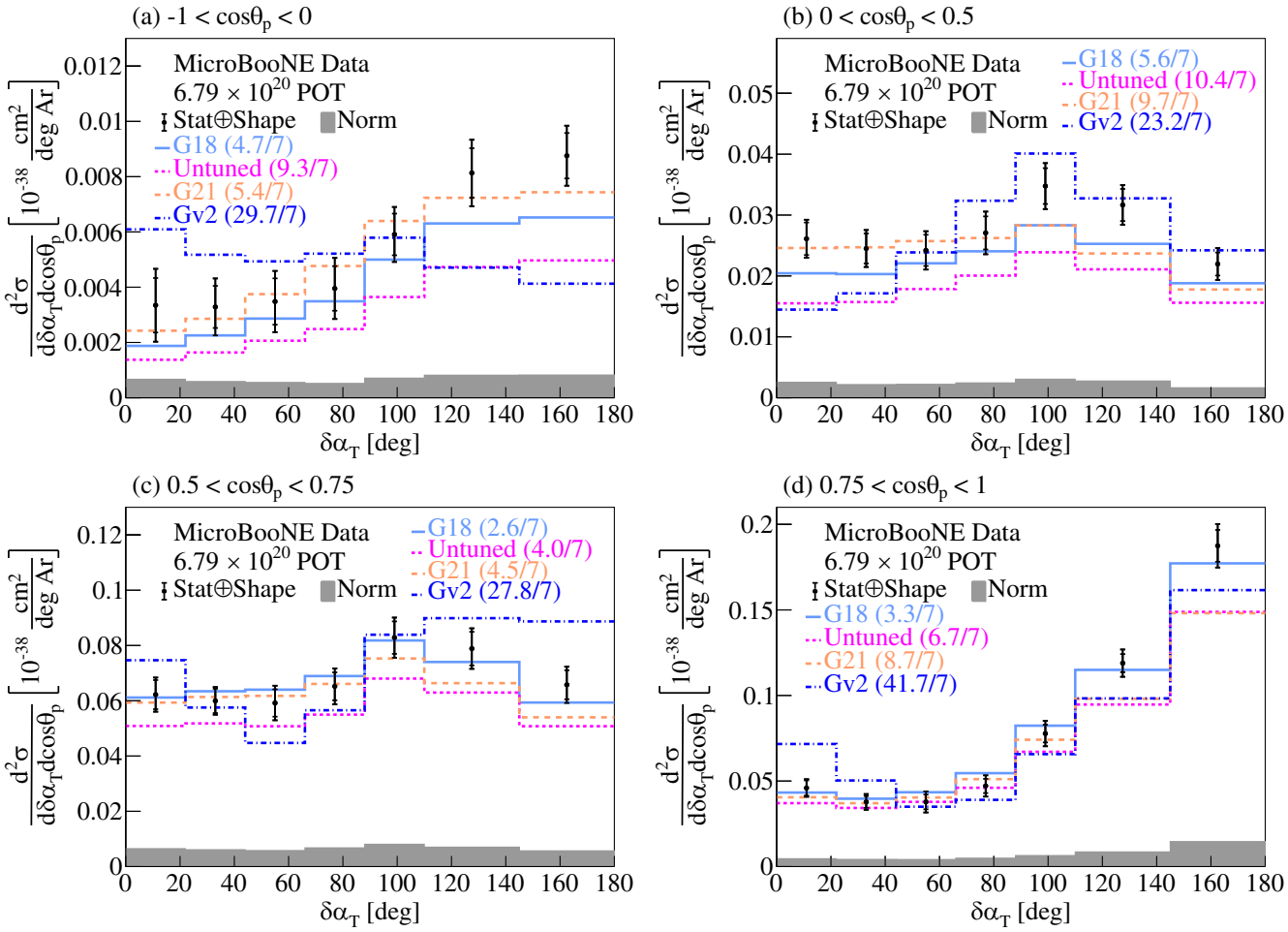

FIG. 29. The flux-integrated double-differential cross sections as a function of $\delta\alpha_T$ in $\cos\theta_p$ bins. Inner and outer error bars show the statistical and total (statistical and shape systematic) uncertainty at the 1σ, or 68%, confidence level. The gray band shows the normalization systematic uncertainty. Colored lines show the results of theoretical cross section calculations using the G18 (light blue), Untuned (magenta), G21 (orange), and Gv2 (dark blue) GENIE configurations. The numbers in parentheses show the χ^2/bins calculation for each one of the predictions.

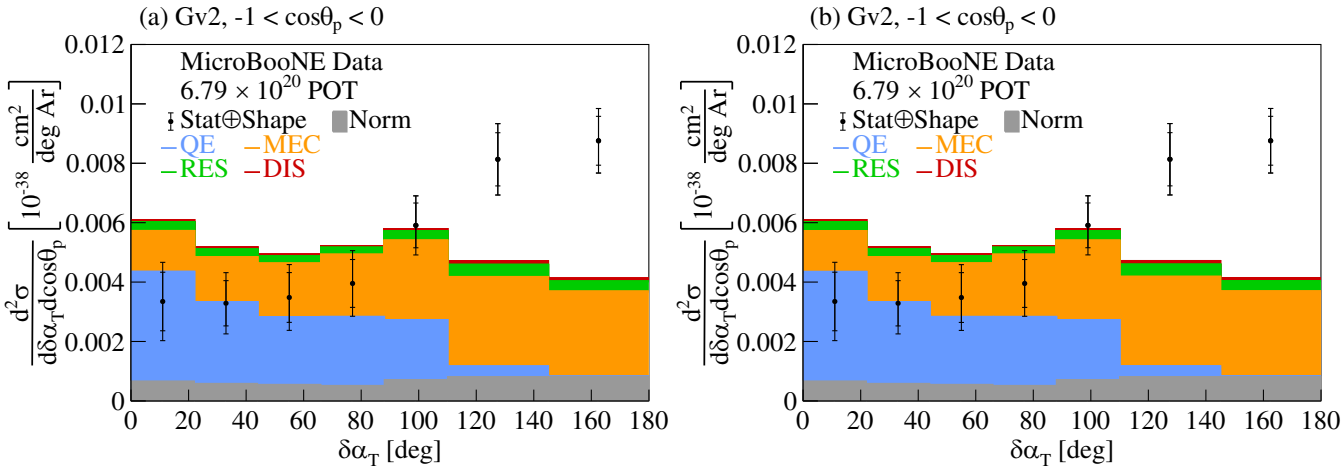

FIG. 30. Comparison between the data flux-integrated double-differential cross section as a function of $\delta\alpha_T$ for events in the region $-1 < \cos\theta_p < 0$ region against the G18 and GENIE predictions. Inner and outer error bars show the statistical and total (statistical and shape systematic) uncertainty at the 1σ, or 68%, confidence level. The gray band shows the normalization systematic uncertainty. Colored stacked histograms show the results of theoretical cross section calculations using the (a) G18 and (b) Gv2 GENIE predictions for QE (blue), MEC (orange), RES (green), and DIS (red) interactions.

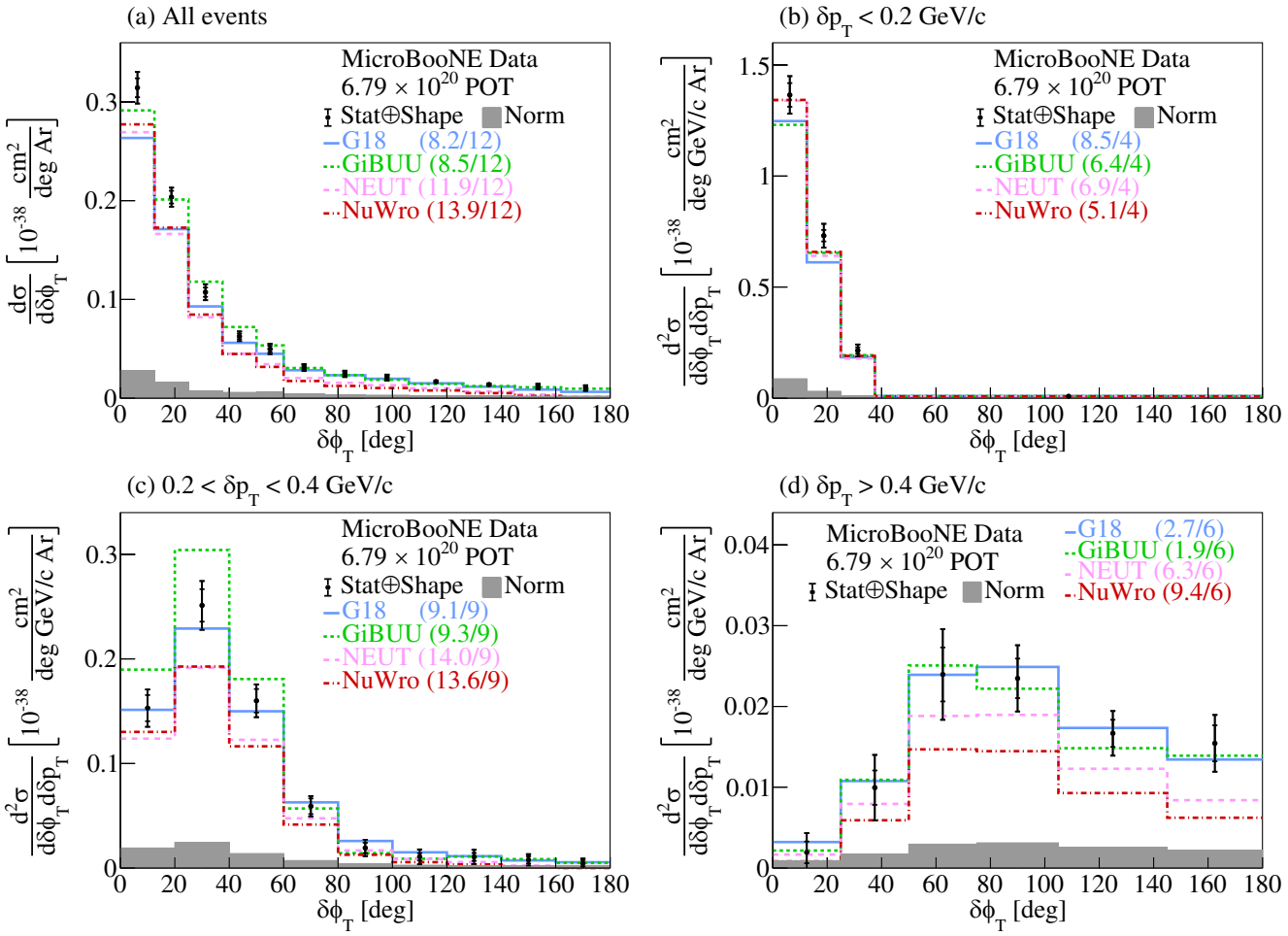

FIG. 31. The flux-integrated (a) single- and (b)–(d) double- (in δp_T bins) differential cross sections as a function of $\delta\phi_T$. Inner and outer error bars show the statistical and total (statistical and shape systematic) uncertainty at the 1σ, or 68%, confidence level. The gray band shows the normalization systematic uncertainty. Colored lines show the results of theoretical cross section calculations using the G18 GENIE (blue), GiBUU (green), NEUT (pink), and NuWro (red) event generators. The numbers in parentheses show the χ^2/bins calculation for each one of the predictions.

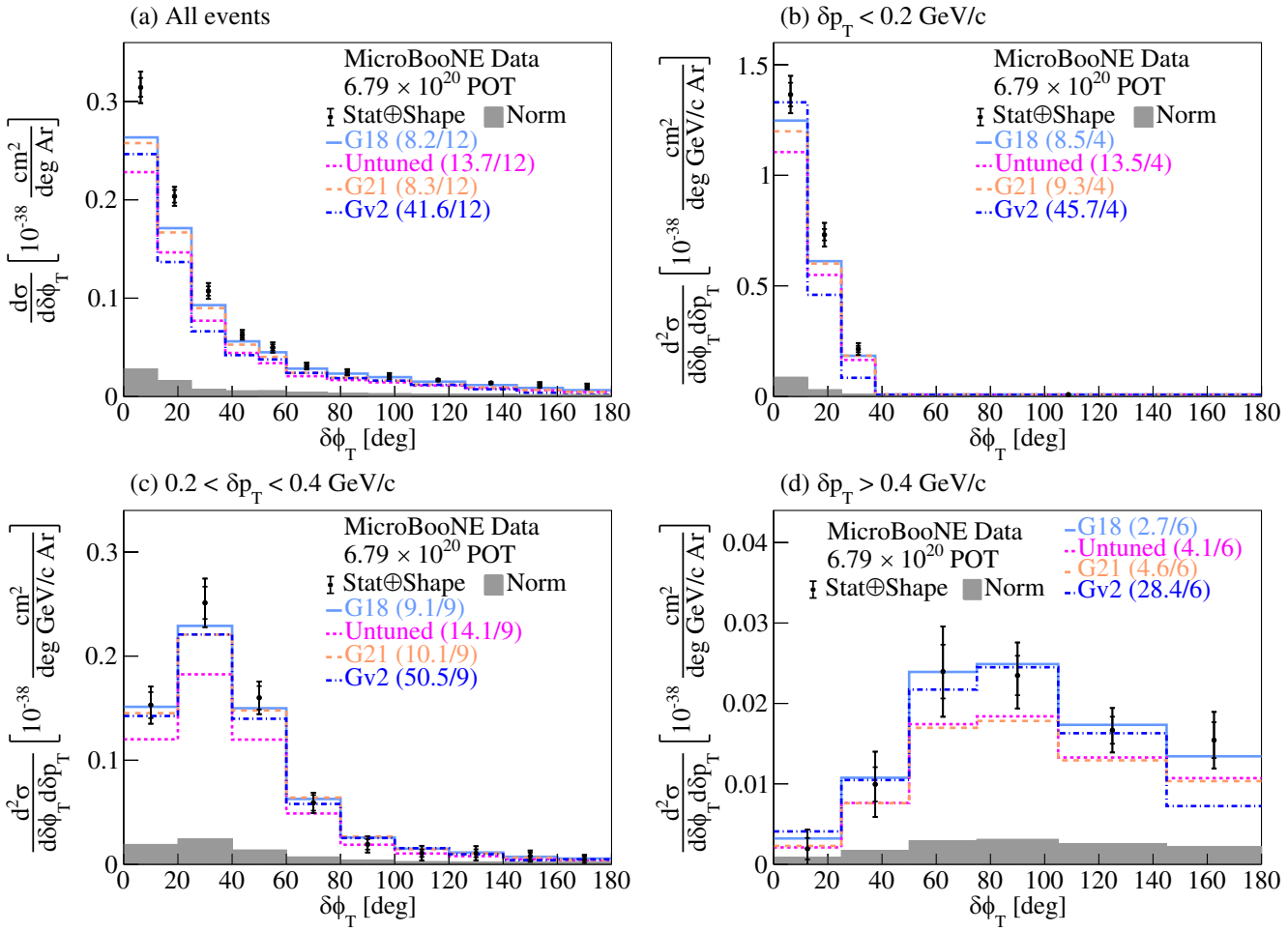

FIG. 32. The flux-integrated (a) single- and (b)–(d) double- (in δp_T bins) differential cross sections as a function of $\delta\phi_T$. Inner and outer error bars show the statistical and total (statistical and shape systematic) uncertainty at the 1σ, or 68%, confidence level. The gray band shows the normalization systematic uncertainty. Colored lines show the results of theoretical cross section calculations using the G18 (light blue), Untuned (magenta), G21 (orange), and Gv2 (dark blue) GENIE configurations. The numbers in parentheses show the χ^2/bins calculation for each one of the predictions.

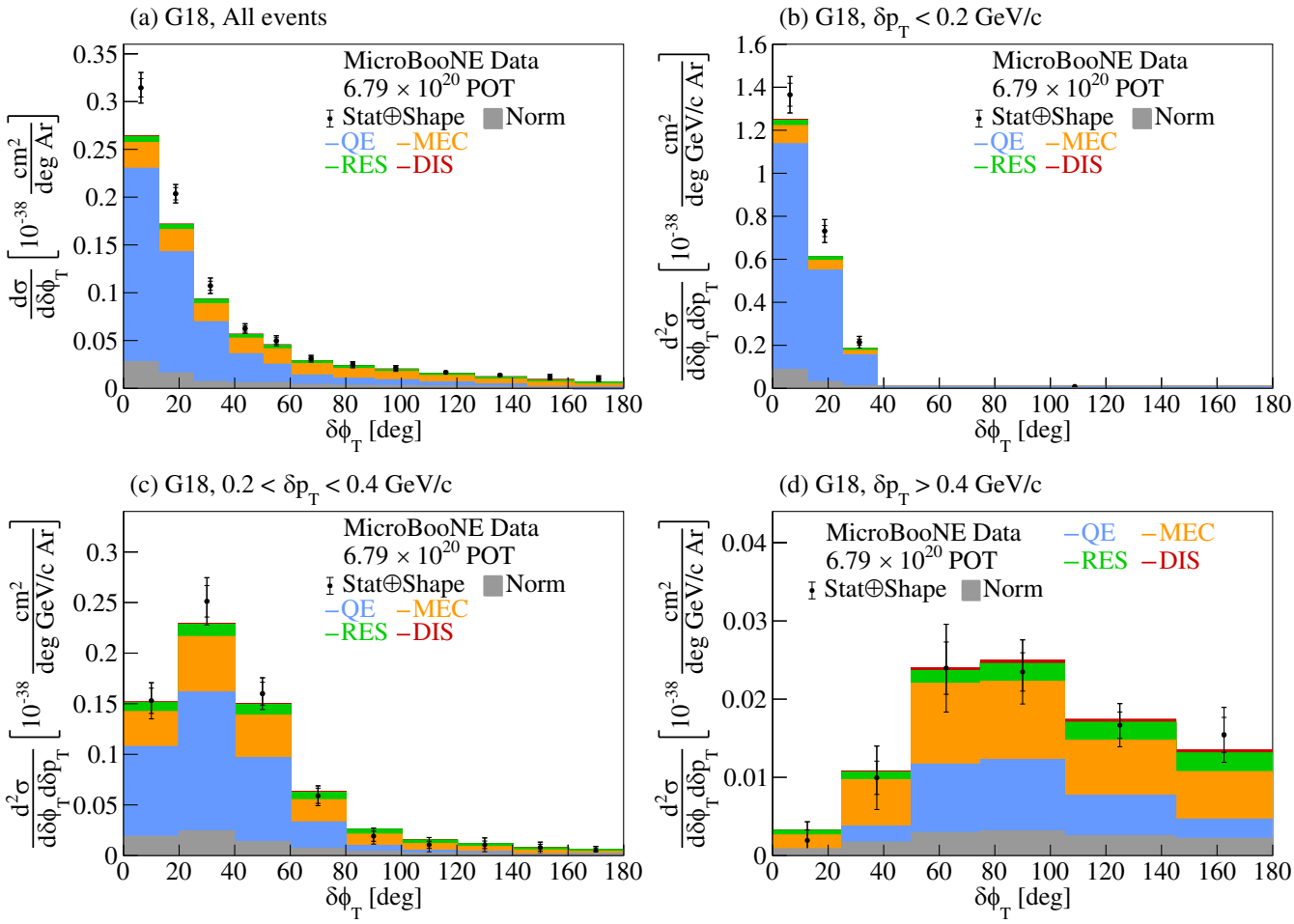

FIG. 33. Comparison between the flux-integrated double- (in δp_T bins) differential cross sections as a function of $\delta\phi_T$ for data and the G18 GENIE prediction. Inner and outer error bars show the statistical and total (statistical and shape systematic) uncertainty at the 1σ, or 68%, confidence level. The gray band shows the normalization systematic uncertainty. Colored stacked histograms show the results of theoretical cross section calculations using the G18 prediction for QE (blue), MEC (orange), RES (green), and DIS (red) interactions.

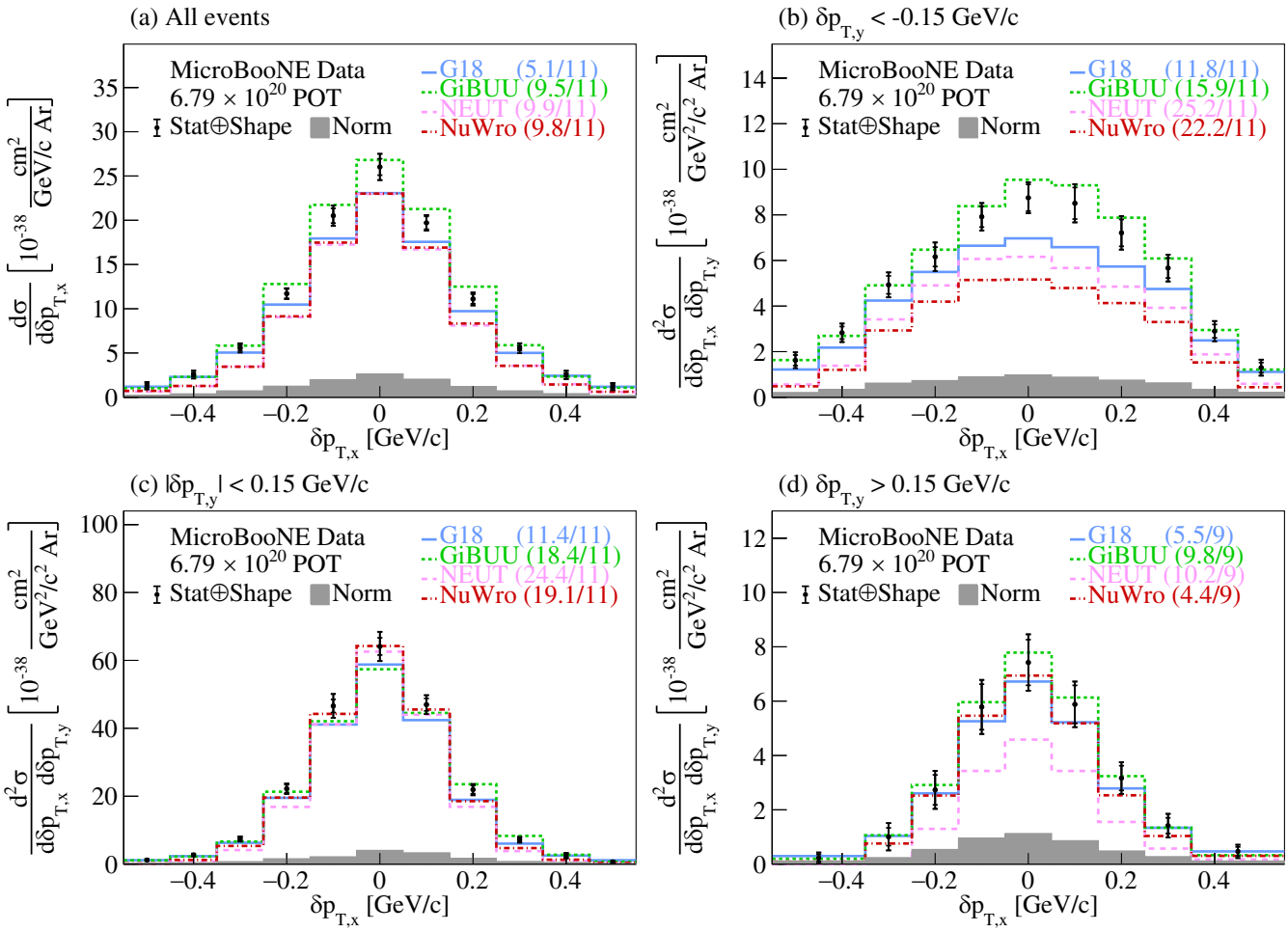

FIG. 34. The flux-integrated (a) single- and (b)–(d) double- (in $\delta p_{T,y}$ bins) differential cross sections as a function of $\delta p_{T,x}$. Inner and outer error bars show the statistical and total (statistical and shape systematic) uncertainty at the 1σ, or 68%, confidence level. The gray band shows the normalization systematic uncertainty. Colored lines show the results of theoretical cross section calculations using the G18 GENIE (blue), GiBUU (green), NEUT (pink), and NuWro (red) event generators. The numbers in parentheses show the χ^2/bins calculation for each one of the predictions.

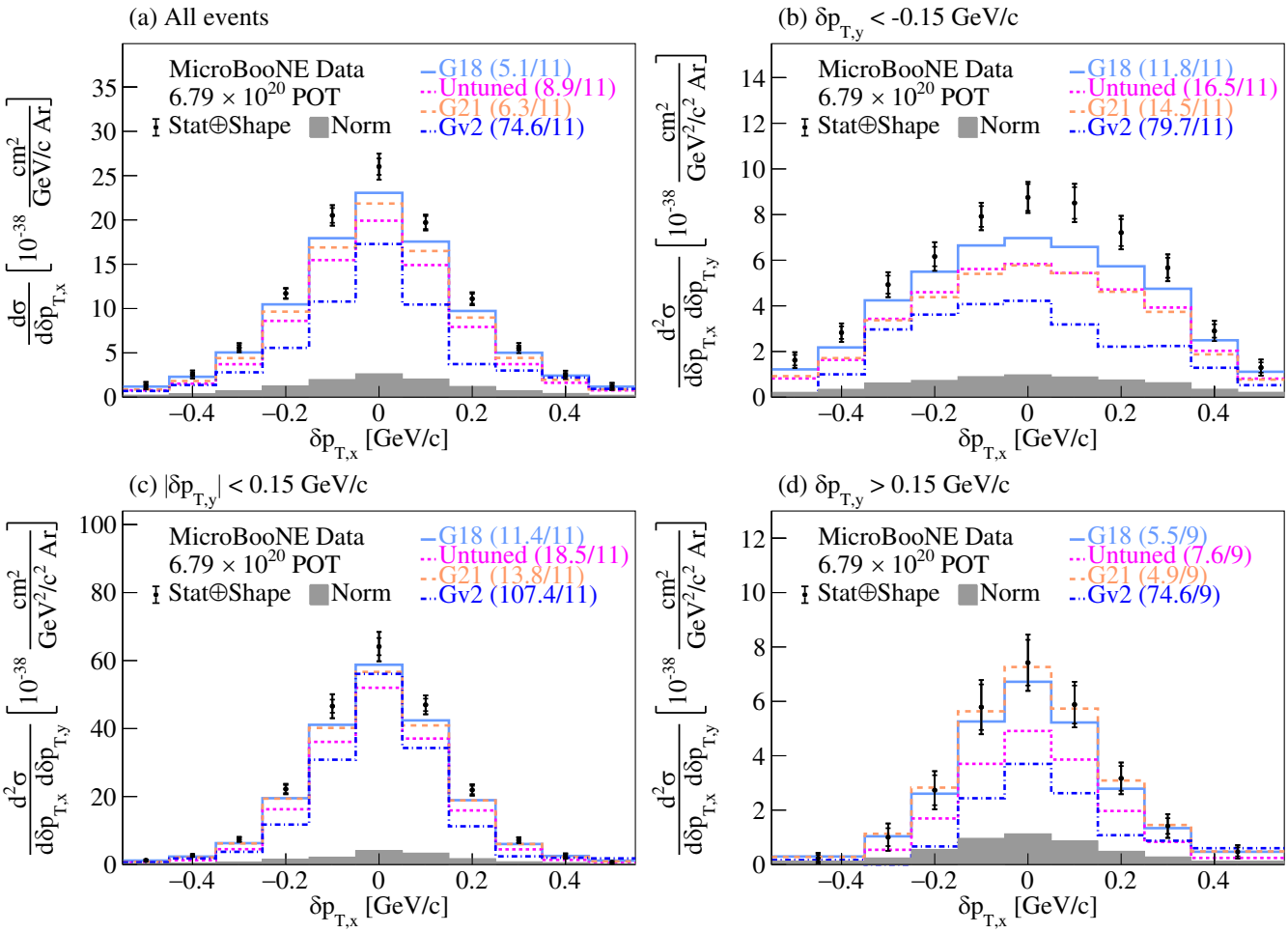

FIG. 35. The flux-integrated (a) single- and (b)–(d) double- (in $\delta p_{T,y}$ bins) differential cross sections as a function of $\delta p_{T,x}$. Inner and outer error bars show the statistical and total (statistical and shape systematic) uncertainty at the 1σ, or 68%, confidence level. The gray band shows the normalization systematic uncertainty. Colored lines show the results of theoretical cross section calculations using the G18 (light blue), Untuned (magenta), G21 (orange), and Gv2 (dark blue) GENIE configurations. The numbers in parentheses show the χ^2/bins calculation for each one of the predictions.

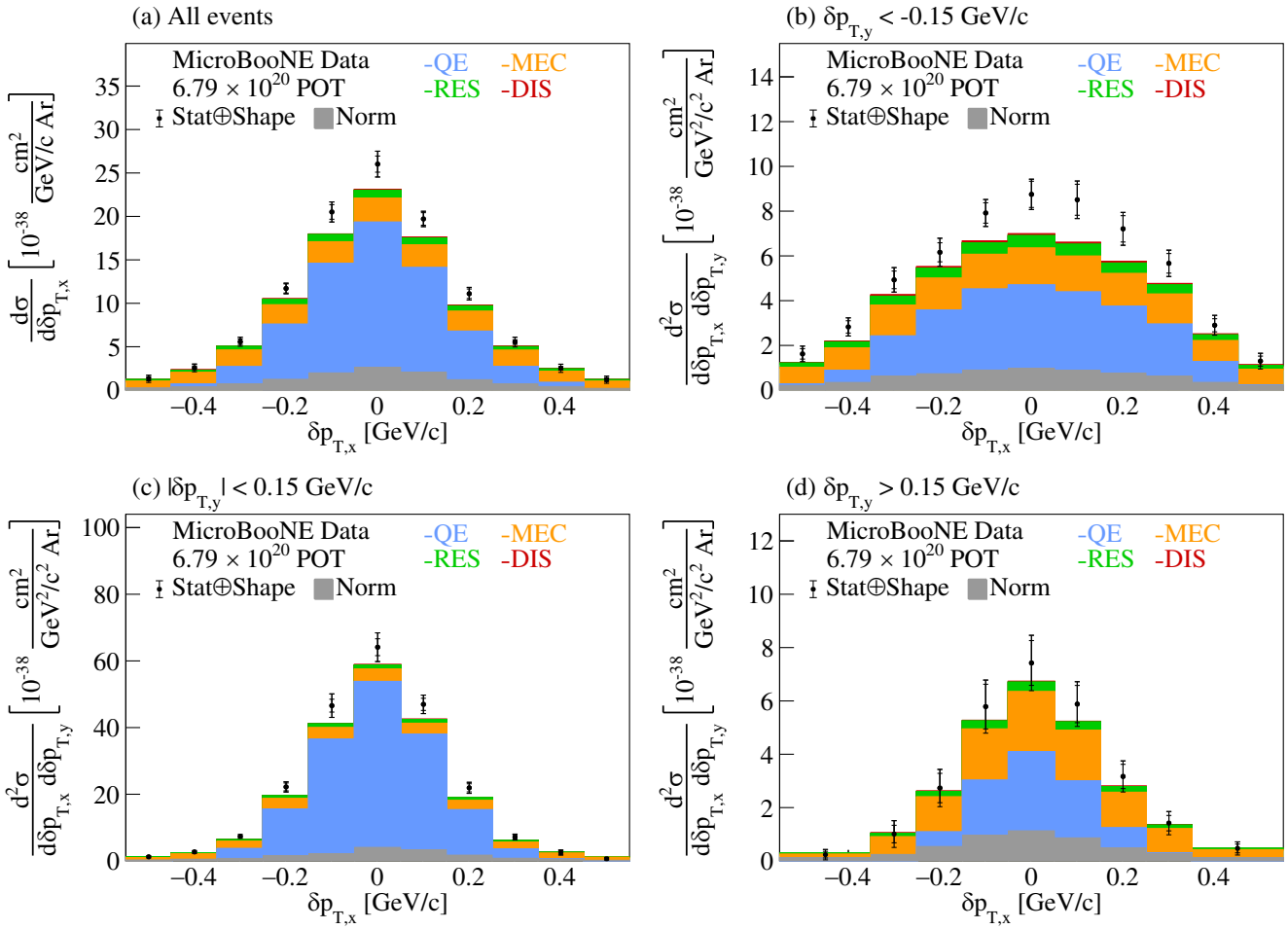

FIG. 36. Comparison between the flux-integrated double- (in $\delta p_{T,y}$ bins) differential cross sections as a function of $\delta p_{T,x}$ for data and the G18 vGENIE prediction. Inner and outer error bars show the statistical and total (statistical and shape systematic) uncertainty at the 1σ, or 68%, confidence level. The gray band shows the normalization systematic uncertainty. Colored stacked histograms show the results of theoretical cross section calculations using the G18 GENIE prediction for QE (blue), MEC (orange), RES (green), and DIS (red) interactions.

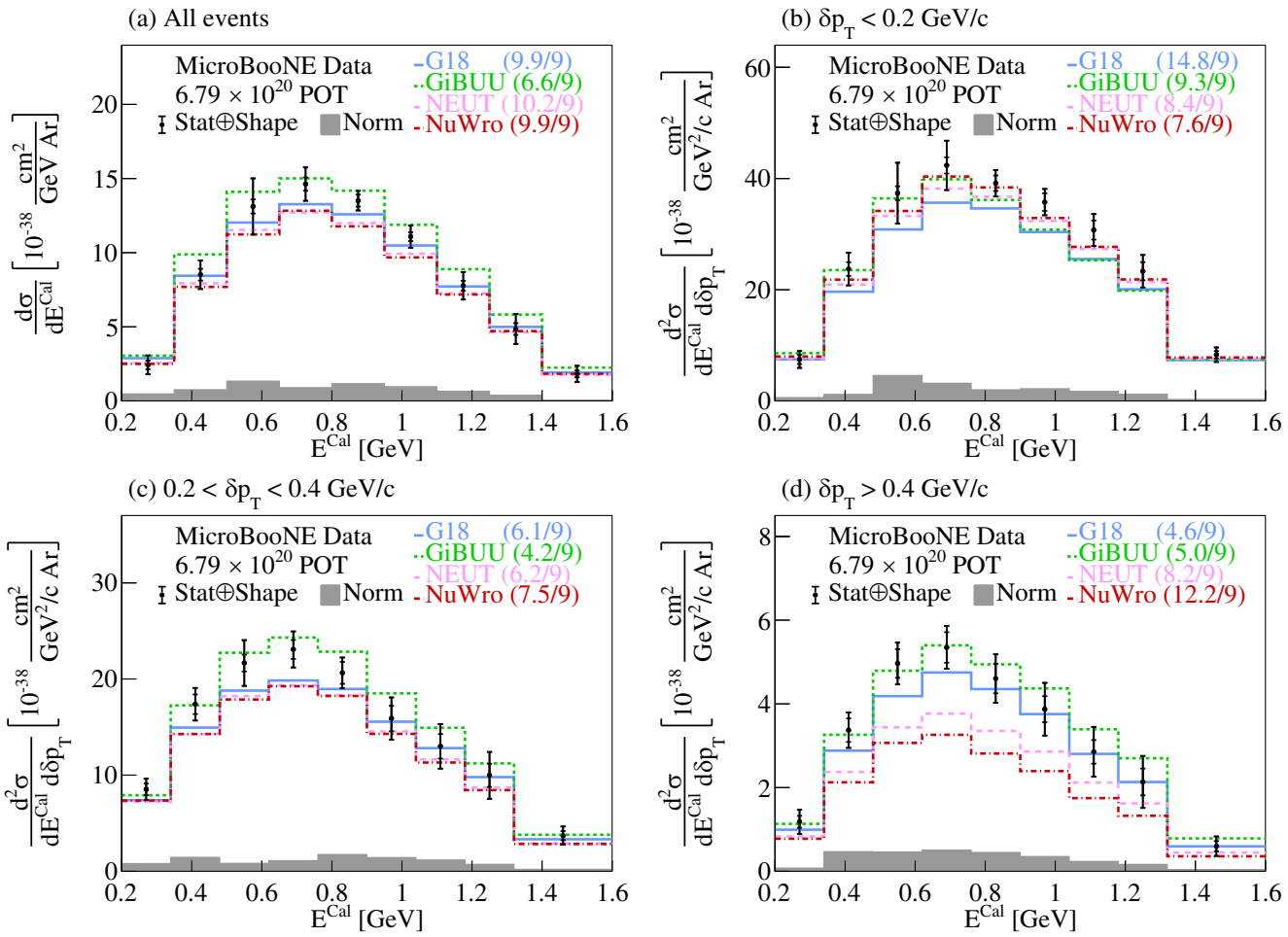

FIG. 37. The flux-integrated (a) single- and (b)–(d) double- (in δp_T bins) differential cross sections as a function of E^{Cal}. Inner and outer error bars show the statistical and total (statistical and shape systematic) uncertainty at the 1σ, or 68%, confidence level. The gray band shows the normalization systematic uncertainty. Colored lines show the results of theoretical cross section calculations using the G18 GENIE (blue), GiBUU (green), NEUT (pink), and NuWro (red) event generators. The numbers in parentheses show the χ^2/bins calculation for each one of the predictions.

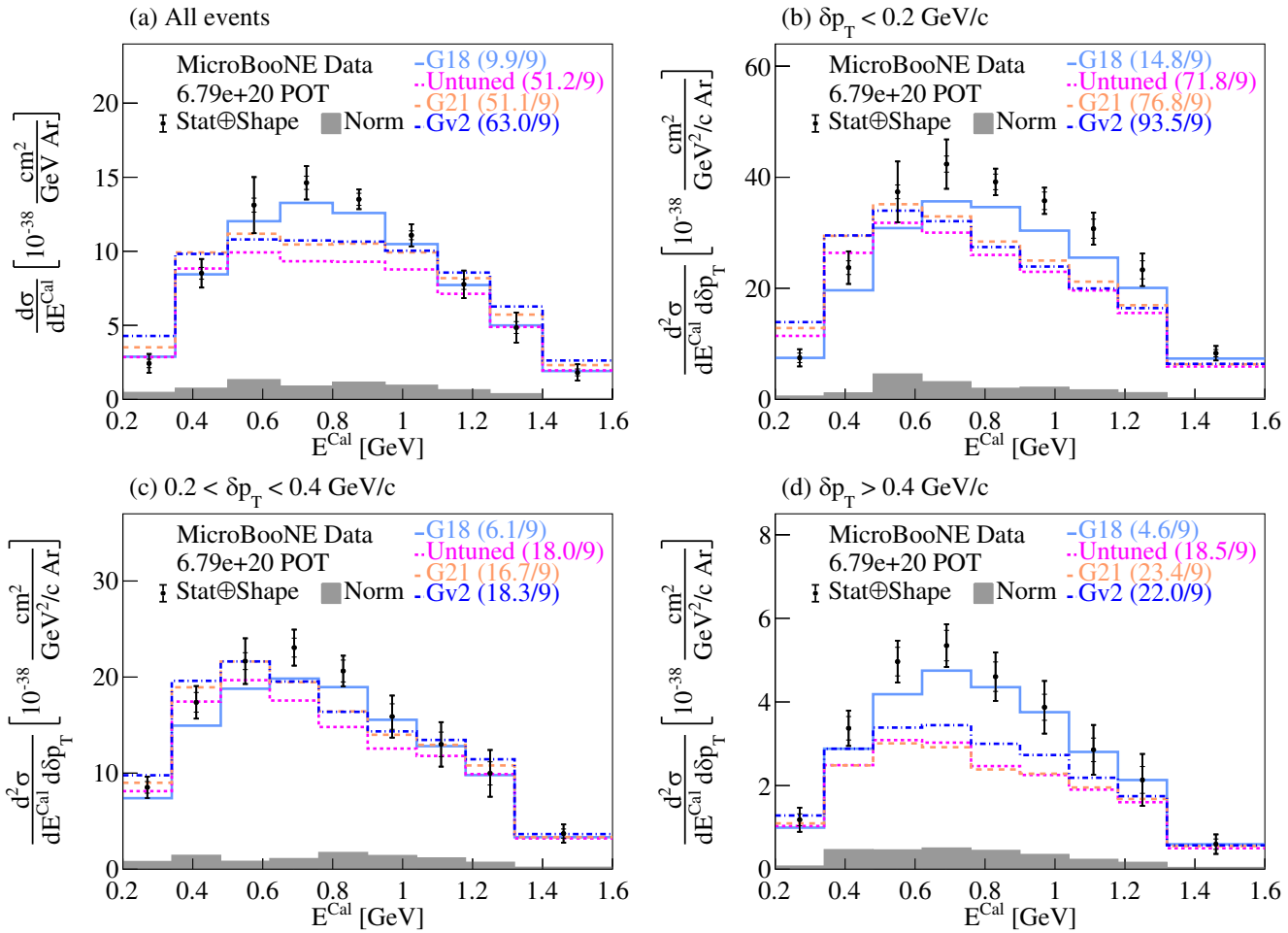

FIG. 38. The flux-integrated (a) single- and (b)–(d) double- (in δp_T bins) differential cross sections as a function of E^{Cal}. Inner and outer error bars show the statistical and total (statistical and shape systematic) uncertainty at the 1σ, or 68%, confidence level. The gray band shows the normalization systematic uncertainty. Colored lines show the results of theoretical cross section calculations using the G18 (light blue), Untuned (magenta), G21 (orange), and Gv2 (dark blue) GENIE configurations.

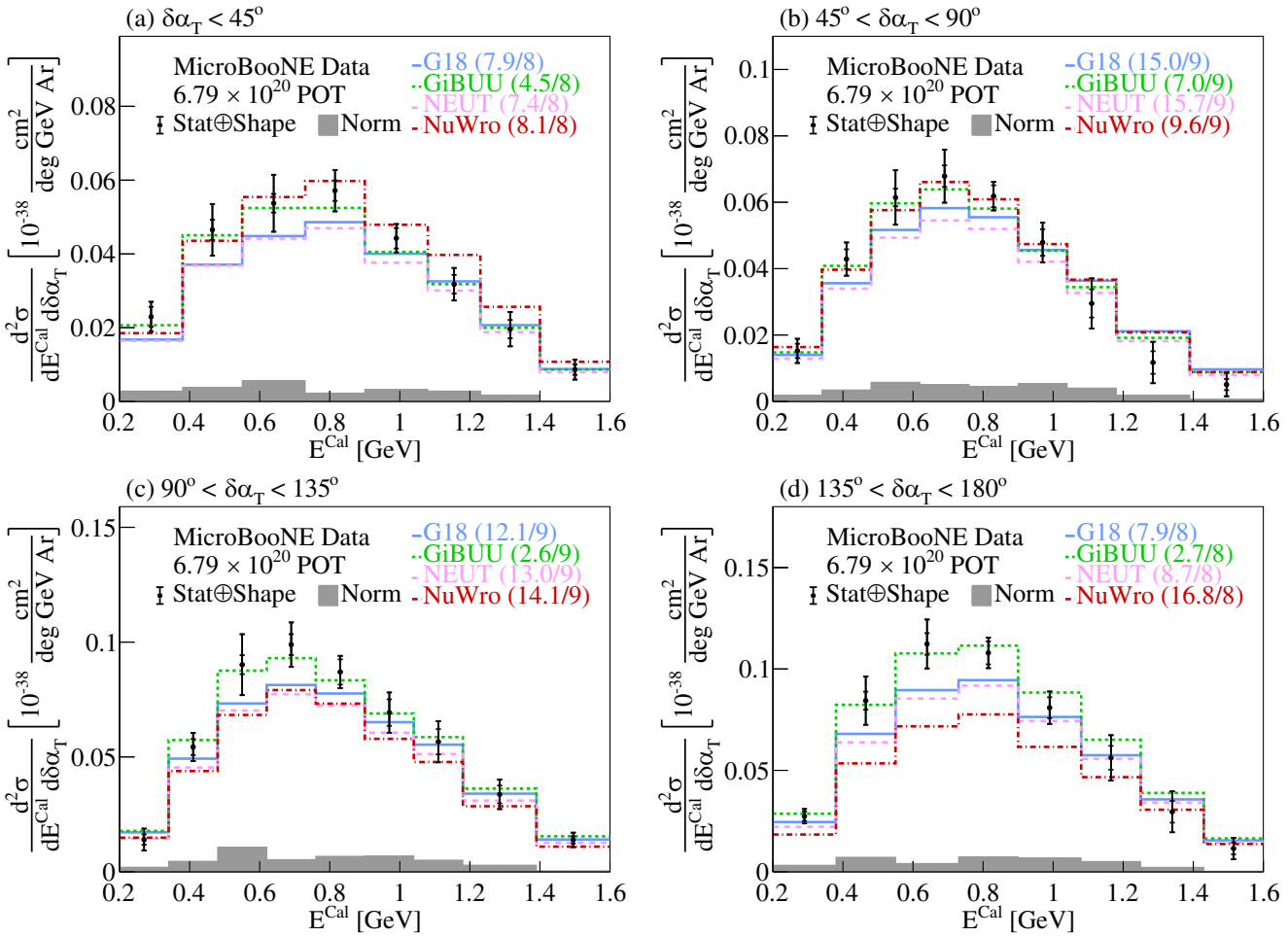

FIG. 39. The flux-integrated double-differential cross sections as a function of E^{Cal} in $\delta\alpha_T$ bins. Inner and outer error bars show the statistical and total (statistical and shape systematic) uncertainty at the 1σ, or 68%, confidence level. The gray band shows the normalization systematic uncertainty. Colored lines show the results of theoretical cross section calculations using the G18 GENIE (blue), GiBUU (green), NEUT (pink), and NuWro (red) event generators. The numbers in parentheses show the χ^2/bins calculation for each one of the predictions.

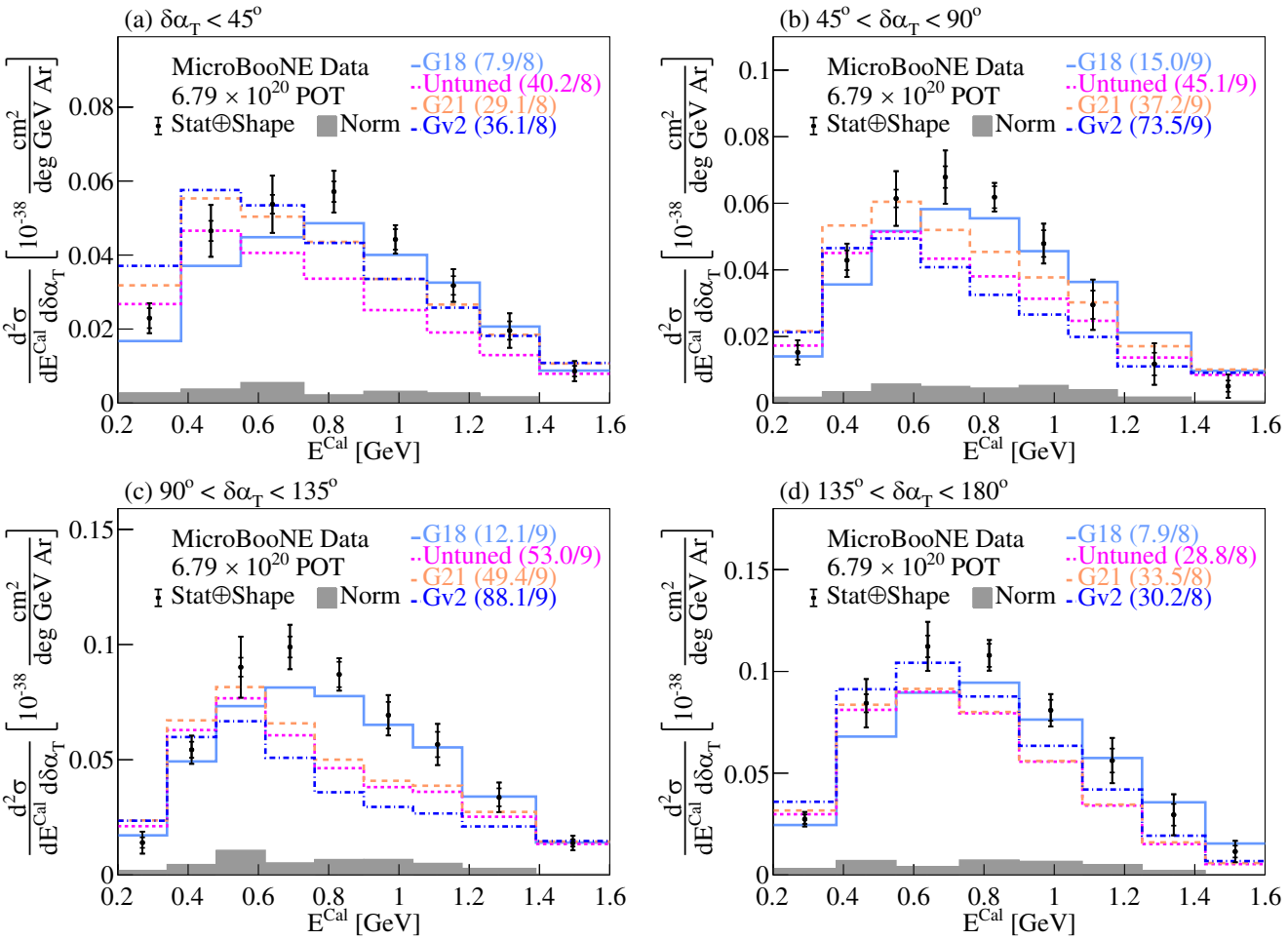

FIG. 40. The flux-integrated double-differential cross sections as a function of E^{Cal} in $\delta\alpha_T$ bins. Inner and outer error bars show the statistical and total (statistical and shape systematic) uncertainty at the 1σ, or 68%, confidence level. The gray band shows the normalization systematic uncertainty. Colored lines show the results of theoretical cross section calculations using the G18 (light blue), Untuned (magenta), G21 (orange), and Gv2 (dark blue) GENIE configurations. The numbers in parentheses show the χ^2/bins calculation for each one of the predictions.

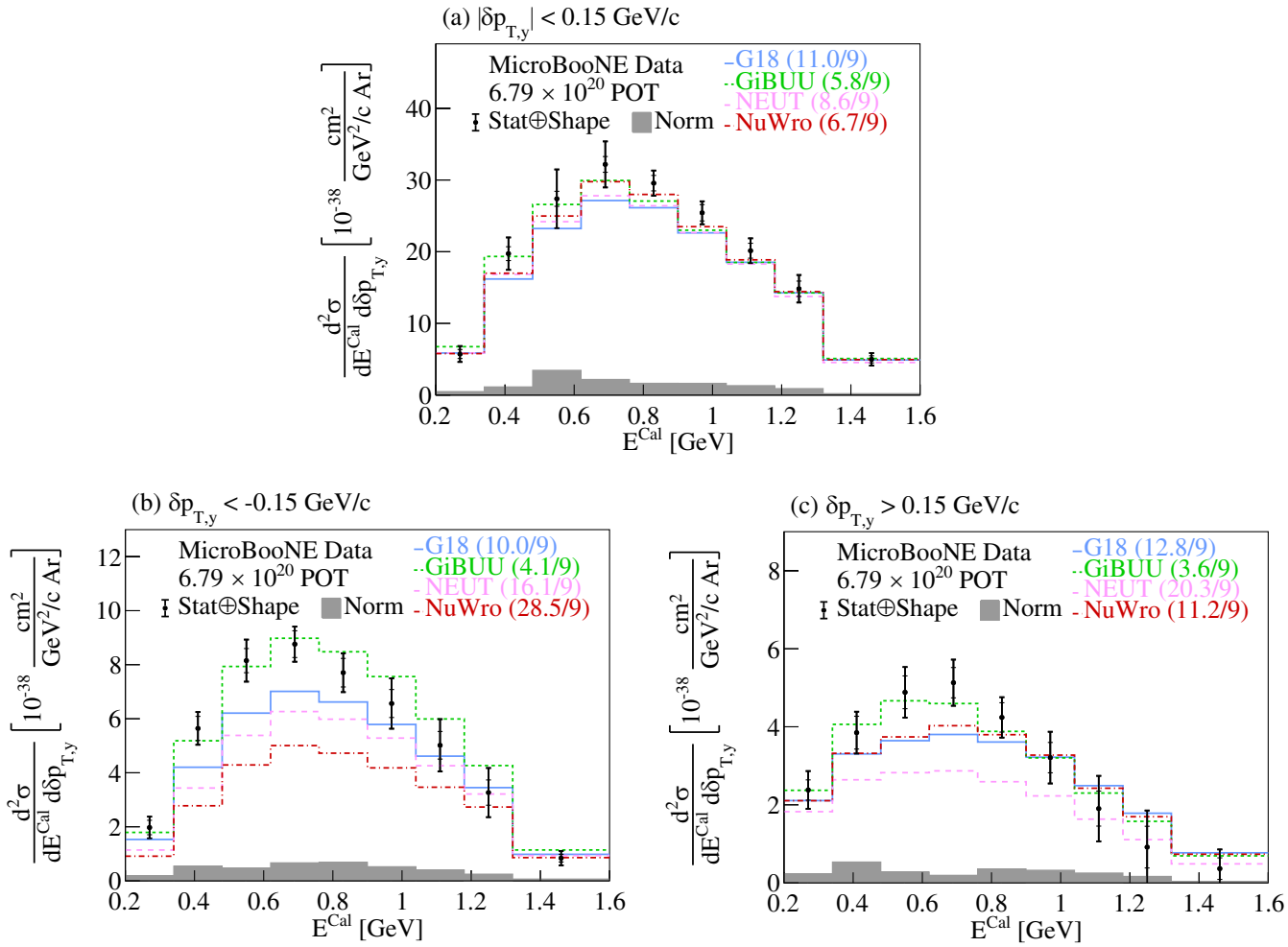

FIG. 41. The flux-integrated double-differential cross sections as a function of E^{Cal} in $\delta p_{T,y}$ bins. Inner and outer error bars show the statistical and total (statistical and shape systematic) uncertainty at the 1σ, or 68%, confidence level. The gray band shows the normalization systematic uncertainty. Colored lines show the results of theoretical cross section calculations using the G18 GENIE (blue), GiBUU (green), NEUT (pink), and NuWro (red) event generators. The numbers in parentheses show the χ^2/bins calculation for each one of the predictions.

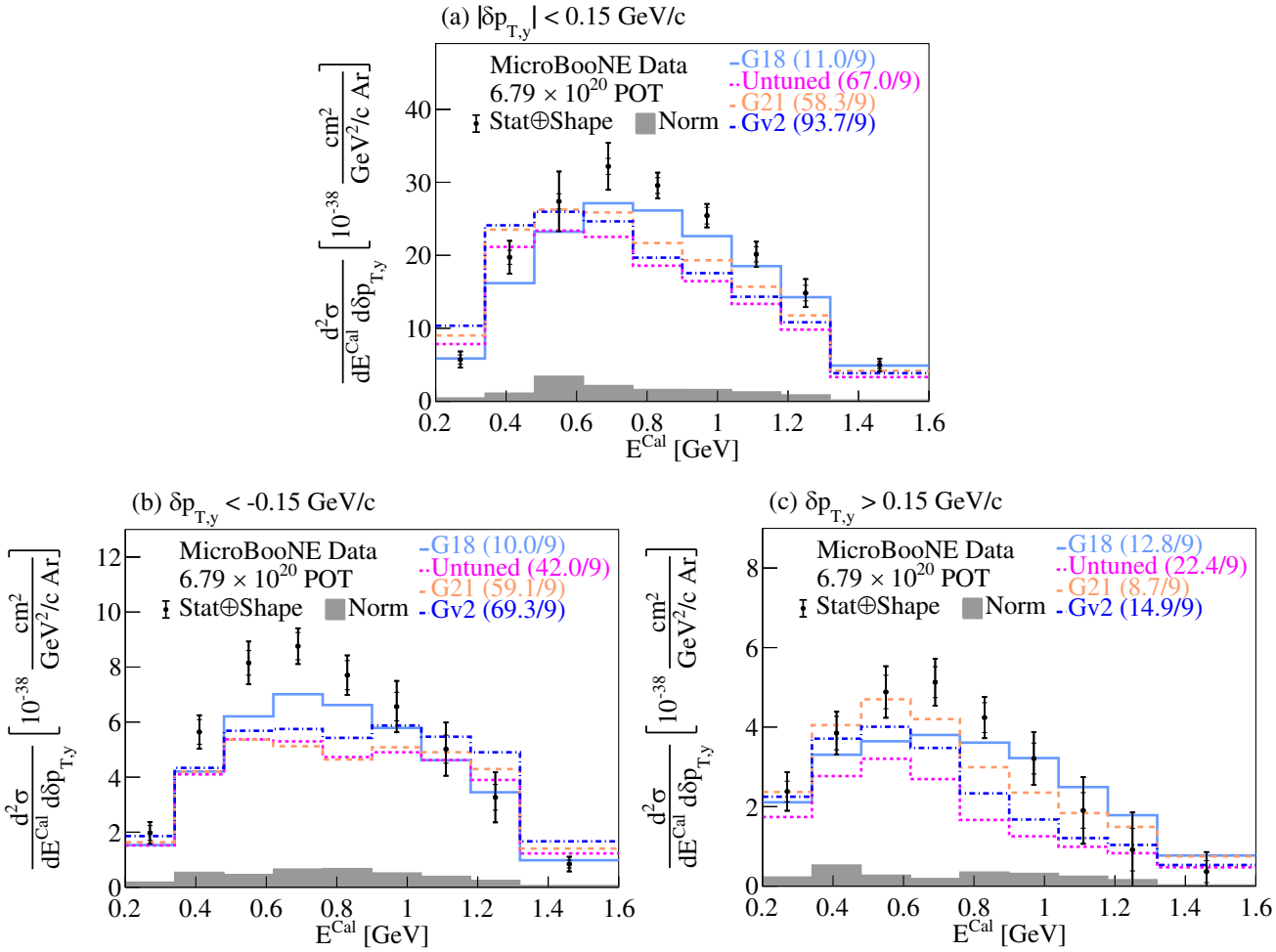

FIG. 42. The flux-integrated double-differential cross sections as a function of E^{Cal} in $\delta p_{T,y}$ bins. Inner and outer error bars show the statistical and total (statistical and shape systematic) uncertainty at the 1σ, or 68%, confidence level. The gray band shows the normalization systematic uncertainty. Colored lines show the results of theoretical cross section calculations using the G18 (light blue), Untuned (magenta), G21 (orange), and Gv2 (dark blue) GENIE configurations. The numbers in parentheses show the χ^2/bins calculation for each one of the predictions.

[1] M. Tanabashi *et al.* (Particle Data Group), Review of particle physics, Phys. Rev. D **98**, 030001 (2018).

[2] K. Abe *et al.* (T2K Collaboration), Constraint on the matter–antimatter symmetry-violating phase in neutrino oscillations, Nature (London) **580**, 339 (2020).

[3] B. Abi *et al.* (DUNE Collaboration), The DUNE far detector interim design report volume 1: Physics, technology and strategies, arXiv:1807.10334.

[4] B. Abi *et al.* (DUNE Collaboration), The DUNE far detector interim design report volume 2: Single-phase module, arXiv:1807.10327.

[5] B. Abi *et al.* (DUNE Collaboration), The DUNE far detector interim design report volume 3: Dual-phasemodule, arXiv:1807.10340.

[6] K. Abe *et al.* (Hyper-Kamiokande Collaboration), Hyper-Kamiokande design report, arXiv:1805.04163.

[7] M. Antonello *et al.* (MicroBooNE, LAr1-ND, ICARUS-WA104 Collaborations), A proposal for a three detector short-baseline neutrino oscillation program in the fermilab booster neutrino beam, arXiv:1503.01520.

[8] F. Tortorici, V. Bellini, and C. Sutera (ICARUS Collaboration), Upgrade of the ICARUS T600 time projection chamber, J. Phys. Conf. Ser. **1056**, 012057 (2018).

[9] B. Abi *et al.* (DUNE Collaboration), Deep underground neutrino experiment (DUNE), far detector technical design report, volume II DUNE physics, arXiv:2002.03005.

[10] S. Dolan, U. Mosel, K. Gallmeister, L. Pickering, and S. Bolognesi, Sensitivity of Neutrino-Nucleus interaction measurements to 2p2h excitations, Phys. Rev. C **98**, 045502 (2018).

[11] N. Rocco, A. Lovato, and O. Benhar, Unified Description of Electron-Nucleus Scattering within the Spectral Function Formalism, Phys. Rev. Lett. **116**, 192501 (2016).

[12] N. Rocco, Ab initio calculations of Lepton-Nucleus scattering, Front. Phys. **8**, 116 (2020).

[13] X.-G. Lu, L. Pickering, S. Dolan, G. Barr, D. Coplowe, Y. Uchida, D. Wark, M. O. Wascko, A. Weber, and T. Yuan, Measurement of nuclear effects in neutrino interactions with minimal dependence on neutrino energy, Phys. Rev. C **94**, 015503 (2016).

[14] K. Abe *et al.* (T2K Collaboration), Characterization of nuclear effects in muon-neutrino scattering on hydrocarbon with a measurement of final-state kinematics and correlations in charged-current pionless interactions at T2K, Phys. Rev. D **98**, 032003 (2018).

[15] X.-G. Lu *et al.* (MINERvA Collaboration), Measurement of Final-State Correlations in Neutrino Muon-Proton Mesonless Production on Hydrocarbon at $E = 3$ GeV, Phys. Rev. Lett. **121**, 022504 (2018).

[16] T. Cai *et al.* (MINERvA Collaboration), Nucleon binding energy and transverse momentum imbalance in neutrino-nucleus reactions, Phys. Rev. D **101**, 092001 (2020).

[17] L. Bathe-Peters, S. Gardiner, and R. Guenette, Comparing generator predictions of transverse kinematic imbalance in neutrino-argon scattering, arXiv:2201.04664.

[18] P. Abratenko *et al.* (MicroBooNE Collaboration), First Measurement of Differential Charged Current Quasielasticlike ν_μ-Argon Scattering Cross Sections with the MicroBooNE Detector, Phys. Rev. Lett. **125**, 201803 (2020).

[19] R. Acciarri *et al.* (MicroBooNE Collaboration), Design and construction of the MicroBooNE detector, J. Instrum. **12**, P02017 (2017).

[20] A. Aguilar-Arevalo *et al.* (MiniBooNE Collaboration), The Neutrino flux prediction at MiniBooNE, Phys. Rev. D **79**, 072002 (2009).

[21] D. Kaleko, PMT triggering and readout for the MicroBooNE experiment, J. Instrum. **8**, C09009 (2013).

[22] R. Acciarri *et al.* (MicroBooNE Collaboration), The Pandora multi-algorithm approach to automated pattern recognition of cosmic-ray muon and neutrino events in the MicroBooNE detector, Eur. Phys. J. C **78**, 82 (2018).

[23] Table 289: Muons in liquid argon (Ar), http://pdg.lbl.gov/2012/AtomicNuclearProperties/MUON_ELOSS_TABLES/muonloss_289.pdf (2012).

[24] S. K. H. Bichsel and D. E. Groom, Passage of particles through matter, PDG Chapter 27, Figure 27.1, http://pdg.lbl.gov/2005/reviews/passagerpp.pdf (2005).

[25] P. Abratenko *et al.* (MicroBooNE Collaboration), First measurement of differential cross sections for muon neutrino charged current interactions on argon with a two-proton final state in the MicroBooNE detector, arXiv:2211.03734.

[26] W. Van De Pontseele, Search for electron neutrino anomalies with the MicroBooNE detector, Ph.D. thesis, Oxford University, 2020.

[27] P. Abratenko *et al.* (MicroBooNE Collaboration), Search for an anomalous excess of charged-current ν_e interactions without pions in the final state with the MicroBooNE experiment, Phys. Rev. D **105**, 112004 (2022).

[28] P. Abratenko *et al.* (MicroBooNE Collaboration), Calorimetric classification of track-like signatures in liquid argon TPCs using MicroBooNE data, J. High Energy Phys. 12 (2021) 153.

[29] See Supplemental Material at http://link.aps.org/supplemental/10.1103/PhysRevD.108.053002 for the data release, the log-likelihood ratio score, the uncertainty components, and the GENIE cross section uncertainties.

[30] M. Berger, J. Coursey, M. Zucker, and J. Chang, Stopping powers and ranges for protons and alpha particles, NIST Standard Reference Database 124, 2017.

[31] P. Abratenko *et al.* (MicroBooNE Collaboration), Determination of muon momentum in the MicroBooNE LArTPC using an improved model of multiple Coulomb scattering, J. Instrum. **12**, P10010 (2017).

[32] C. Adams *et al.* (MicroBooNE Collaboration), Rejecting cosmic background for exclusive charged current quasi elastic neutrino interaction studies with Liquid Argon TPCs; a case study with the MicroBooNE detector, Eur. Phys. J. C **79**, 673 (2019).

[33] P. Abratenko *et al.* (MicroBooNE Collaboration), First Measurement of Energy-Dependent Inclusive Muon Neutrino Charged-Current Cross Sections on Argon with the MicroBooNE Detector, Phys. Rev. Lett. **128**, 151801 (2022).

[34] P. Abratenko *et al.* (MicroBooNE Collaboration), First measurement of inclusive electron-neutrino and antineutrino charged current differential cross sections in charged lepton energy on argon in MicroBooNE, Phys. Rev. D **105**, L051102 (2022).

[35] C. Andreopoulos *et al.*, The GENIE Neutrino Monte Carlo generator, Nucl. Instrum. Methods Phys. Res., Sect. A **614**, 87 (2010).

[36] C. Andreopoulos *et al.*, The GENIE neutrino monte carlo generator: Physics and user manual, arXiv:1510.05494.

[37] K. Abe *et al.* (T2K Collaboration), Measurement of double-differential muon neutrino charged-current interactions on C_8H_8 without pions in the final state using the T2K off-axis beam, Phys. Rev. D **93**, 112012 (2016).

[38] P. Abratenko *et al.* (MicroBooNE Collaboration), New CC0π GENIE model tune for MicroBooNE, Phys. Rev. D **105**, 072001 (2022).

[39] S. Agostinelli *et al.* (GEANT4 Collaboration), GEANT4—a simulation toolkit, Nucl. Instrum. Methods Phys. Res., Sect. A **506**, 250 (2003).

[40] R. Pordes and E. Snider, The liquid argon software toolkit (LArSoft): Goals, status and plan, Proc. Sci. ICHEP2016 (**2016**) 182.

[41] E. Snider and G. Petrillo, LArSoft: Toolkit for simulation, reconstruction and analysis of liquid argon TPC neutrino detectors, J. Phys. Conf. Ser. **898**, 042057 (2017).

[42] A. Bodek and T. Cai, Removal energies and final state interaction in lepton nucleus scattering, Eur. Phys. J. C **79**, 293 (2019).

[43] W. Tang, X. Li, X. Qian, H. Wei, and C. Zhang, Data unfolding with Wiener-SVD method, J. Instrum. **12**, P10002 (2017).

[44] A. Aguilar-Arevalo *et al.* (MiniBooNE Collaboration), First measurement of the muon antineutrino double-differential charged-current quasielastic cross section, Phys. Rev. D **88**, 032001 (2013).
[45] J. Calcutt, C. Thorpe, K. Mahn, and L. Fields, Geant4Reweight: A framework for evaluating and propagating hadronic interaction uncertainties in Geant4, J. Instrum. **16**, P08042 (2021).
[46] B. Roe, Statistical errors in Monte Carlo estimates of systematic errors, Nucl. Instrum. Methods Phys. Res., Sect. A **570**, 159 (2007).
[47] T. Golan, J. Sobczyk, and J. Żmuda, NuWro: The Wrocław Monte Carlo Generator of Neutrino Interactions, Nucl. Phys. B, Proc. Suppl. **229–232**, 499 (2012).
[48] P. Abratenko *et al.* (MicroBooNE Collaboration), Novel approach for evaluating detector-related uncertainties in a LArTPC using MicroBooNE data, Eur. Phys. J. C **82**, 454 (2022).
[49] K. Mahn, A search for muon neutrino and antineutrino disappearance in the Booster Neutrino Beam, Ph.D. thesis, Columbia University, 2009.
[50] R. Carrasco and E. Oset, Interaction of Real Photons With Nuclei From 100-MeV to 500-MeV, Nucl. Phys. **A536**, 445 (1992).
[51] J. Nieves, F. Sanchez, I. Ruiz Simo, and M. Vicente Vacas, Neutrino energy reconstruction and the shape of the CCQE-like total cross section, Phys. Rev. D **85**, 113008 (2012).
[52] J. Engel, Approximate treatment of lepton distortion in charged current neutrino scattering from nuclei, Phys. Rev. C **57**, 2004 (1998).
[53] J. Nieves, J. E. Amaro, and M. Valverde, Inclusive quasielastic charged-current neutrino-nucleus reactions, Phys. Rev. C **70**, 055503 (2004).
[54] J. Schwehr, D. Cherdack, and R. Gran, GENIE implementation of IFIC Valencia model for QE-like 2p2h neutrino-nucleus cross section, arXiv:1601.02038.
[55] J. A. Nowak (MiniBooNE Collaboration), Four Momentum Transfer Discrepancy in the Charged Current π^+ Production in the MiniBooNE: Data vs. Theory, AIP Conf. Proc. **1189**, 243 (2009).
[56] K. Kuzmin, V. Lyubushkin, and V. Naumov, Lepton polarization in neutrino nucleon interactions, Phys. Part. Nucl. **35**, S133 (2004).
[57] C. Berger and L. Sehgal, Lepton mass effects in single pion production by neutrinos, Phys. Rev. D **76**, 113004 (2007).
[58] K. M. Graczyk and J. T. Sobczyk, Form factors in the quark resonance model, Phys. Rev. D **77**, 053001 (2008); **79**, 079903(E) (2009).
[59] C. Berger and L. Sehgal, PCAC and coherent pion production by low energy neutrinos, Phys. Rev. D **79**, 053003 (2009).
[60] D. Ashery, I. Navon, G. Azuelos, H. Walter, H. Pfeiffer, and F. Schleputz, True absorption and scattering of pions on nuclei, Phys. Rev. C **23**, 2173 (1981).
[61] U. Mosel, Neutrino event generators: foundation, status and future, Phys. Rev. G **46**, 113001 (2019).
[62] T. Leitner, L. Alvarez-Ruso, and U. Mosel, Charged current neutrino nucleus interactions at intermediate energies, Phys. Rev. C **73**, 065502 (2006).
[63] T. Sjostrand, S. Mrenna, and P. Z. Skands, PYTHIA 6.4 physics and manual, J. High Energy Phys. 05 (2006) 026.
[64] C. Llewellyn Smith, Neutrino reactions at accelerator energies, Phys. Rep. **3**, 261 (1972).
[65] J. Nieves, I. R. Simo, and M. J. V. Vacas, Inclusive charged-current neutrino-nucleus reactions, Phys. Rev. C **83**, 045501 (2011).
[66] T. Katori, Meson exchange current (MEC) models in neutrino interaction generators, AIP Conf. Proc. **1663**, 030001 (2015).
[67] D. Rein and L. Sehgal, Neutrino Excitation of Baryon Resonances and Single Pion Production, Ann. Phys. (N.Y.) **133**, 79 (1981).
[68] S. Mashnik, A. Sierk, K. Gudima, and M. Baznat, CEM03 and LAQGSM03: New modeling tools for nuclear applications, J. Phys. Conf. Ser. **41**, 340 (2006).
[69] S. Dolan, G. D. Megias, and S. Bolognesi, Implementation of the SuSAv2-meson exchange current 1p1h and 2p2h models in GENIE and analysis of nuclear effects in T2K measurements, Phys. Rev. D **101**, 033003 (2020).
[70] S. Dytman, Y. Hayato, R. Raboanary, J. T. Sobczyk, J. Tena-Vidal, and N. Vololoniaina, Comparison of validation methods of simulations for final state interactions in hadron production experiments, Phys. Rev. D **104**, 053006 (2021).
[71] P. Abratenko *et al.* (MicroBooNE Collaboration), First Measurement of Inclusive Muon Neutrino Charged Current Differential Cross Sections on Argon at $E_\nu \sim 0.8$ GeV with the MicroBooNE Detector, Phys. Rev. Lett. **123**, 131801 (2019).
[72] P. Abratenko *et al.* (MicroBooNE Collaboration), Measurement of differential cross sections for ν_μ-Ar charged-current interactions with protons and no pions in the final state with the MicroBooNE detector, Phys. Rev. D **102**, 112013 (2020).
[73] M. B. Avanzini *et al.*, Comparisons and challenges of modern neutrino-scattering experiments, Phys. Rev. D **105**, 092004 (2022).
[74] P. Abratenko *et al.*, companion Letter, First Double-Differential Measurement of Kinematic Imbalance in Neutrino Interactions with the MicroBooNE Detector, Phys. Rev. Lett. **131**, 101802 (2023).